Kinematic and Thermodynamic Structures of Sierra Barrier Jets and Overrunning Atmospheric Rivers during a Landfalling Winter Storm in Northern California

DAVID E. KINGSMILL

University of Colorado, Cooperative Institute for Research in Environmental Sciences, and NOAA/Earth System Research Laboratory, Boulder, Colorado

PAUL J. NEIMAN

NOAA/Earth System Research Laboratory, Boulder, Colorado

BENJAMIN J. MOORE AND MIMI HUGHES

University of Colorado, Cooperative Institute for Research in Environmental Sciences, and NOAA/Earth System Research Laboratory, Boulder, Colorado

SANDRA E. YUTER

North Carolina State University, Raleigh, North Carolina

F. MARTIN RALPH

NOAA/Earth System Research Laboratory, Boulder, Colorado

(Manuscript received 21 September 2012, in final form 16 November 2012)

ABSTRACT

This study characterizes kinematic and thermodynamic structures of Sierra barrier jets (SBJs), atmospheric rivers (ARs), and their interaction over the period 14–16 February 2011 when a winter storm made landfall in northern California. A suite of scanning and profiling Doppler radars, rawinsondes, and GPS receivers is used to document these structures across the Central Valley and up the western Sierra slope to the crest along an ~200-km segment of the Sierra. The winter storm is grouped into two episodes, each having an AR that made landfall. Low-level winds in the SBJ observed during episode 1 were southeasterly and embedded in a stably stratified air mass. Along-barrier wind speeds U_{340} reached maximum values of 25–30 m s^{-1}, as low as ~0.2 km MSL over the Central Valley, and as high as ~1.5 km MSL over the western Sierra slope. Southwesterly winds associated with the AR overlaid the SBJ along an interface that sloped upward from southwest to northeast with a southwestern extent at the western edge of the Central Valley. In contrast, low-level winds in the SBJ observed during episode 2 were more southerly and embedded in a less stable air mass. The U_{340} reached maximum values that were slightly weaker (~20–25 m s^{-1}) and spread over a thicker layer that extended to higher levels over the western Sierra (~2.5 km MSL). Southwesterly winds associated with the AR overlaying the SBJ tilted upward from southwest to northeast with a steeper slope but did not extend as far southwest.

1. Introduction

The vast majority of precipitation that falls along the U.S. West Coast occurs during the cool-season months of October through May. This precipitation occurs in association with extratropical cyclones that form upstream over the Pacific Ocean and ultimately make landfall. A narrow corridor of enhanced water vapor transport is often located within the warm conveyor belt (e.g., Browning 1990; Carlson 1998) present in many midlatitude cyclones. These corridors, referred to as atmospheric rivers (ARs) are focused along the low-level jet (LLJ) in the warm sector, immediately in advance of the cold front (Zhu and Newell 1998; Ralph

Corresponding author address: David E. Kingsmill, University of Colorado, CIRES, UCB 216, Boulder, CO 80309.
E-mail: david.kingsmill@colorado.edu

DOI: 10.1175/MWR-D-12-00277.1

et al. 2004; Neiman et al. 2008). Although low-level stratification within ARs offshore is usually moist neutral (Ralph et al. 2005a), stable stratification is often present at low levels immediately along the coast and in the valleys just inland of the coast (e.g., Neiman et al. 2002, 2006). In the Northern Hemisphere, a stably stratified airstream approaching a mountain barrier slows down and is deflected leftward as a result of a weakened Coriolis force when the Froude number of that airstream is greater than zero but less than one (Pierrehumbert and Wyman 1985; Smolarkiewicz and Rotunno 1990).

Barrier jets often form in association with low-level airflow blocking. These jets are characterized by a wind direction that parallels the long axis of a barrier and a terrain-parallel component of wind speed that exhibits a local maximum in the layer below the barrier crest. Barrier jet flows have been documented across many portions of western North America such as coastal Alaska and British Columbia (e.g., Overland and Bond 1995; Yu and Bond 2002; Loescher et al. 2006; Olson et al. 2007; Olson and Colle 2009), coastal Oregon (e.g., Braun et al. 1997; Yu and Smull 2000;), coastal California (e.g., Doyle 1997; Neiman et al. 2002, 2004) and along the western slope of California's Sierra Nevada (Sierra; e.g., Parish 1982; Marwitz 1983). The barrier jet in the last of these locales, the Sierra barrier jet (SBJ), is important because of its potential to influence the distribution of precipitation along the Sierra, which has an impact on water supply, power generation and flood risk across California. For example, Lundquist et al. (2010) discovered that knowledge of SBJ height was critical for predicting the orographic precipitation gradient across the Sierra. Galewsky and Sobel (2005) found that the SBJ acted as a dynamic barrier along the windward slope of the northern Sierra and thus contributed to flooding rains there. Reeves et al. (2008) discovered that the SBJ may have enhanced precipitation along a prominent westward jog in the northern Sierra because the SBJ encountered the terrain slope at a more perpendicular angle at that locale. Finally, Smith et al. (2010) documented the occurrence of a strong SBJ at the base of the Sierra that contributed to the northward water vapor flux and possible enhancement of precipitation in the northern Sierra during the landfall of an AR.

Observed structural details about the SBJ were first documented during the Sierra Cooperative Pilot Project (SCPP; Reynolds and Dennis 1986). Parish (1982) and Marwitz (1983, 1987) investigated seven storms by analyzing data from a combination of rawinsondes, a research aircraft, and a scanning C-band Doppler radar. They observed blocking of low-level cross-barrier flow over the lower windward slope of the Sierra and maximum terrain-parallel wind speeds of 15–30 m s^{-1} at ~1 km above the windward base of the Sierra. To broaden these cases study results, Smutz (1986) analyzed 1849 rawinsonde-derived wind profiles from a SCPP site near the base of the Sierra over seven cool seasons. The maximum terrain-parallel wind speeds of SBJs identified in these profiles occurred on average at 1.12 km MSL and had a mean value of 11.0 m s^{-1}, with maximum values of ~40–45 m s^{-1}. Recently, Neiman et al. (2010) performed a similar analysis with 915-MHz wind profiler data from a site near the base of the Sierra slightly north of the site used by Smutz (1986) and another site nearby along the lower windward slope of the Sierra at an elevation of 0.69 km MSL. Results of the analysis for the site near the base of the Sierra were comparable with those of Smutz (1986). However, differences were evident for the site along the lower windward Sierra slope where the SBJ occurred on average at 1.82 km MSL. Notably, this is at 1.13 km AGL, approximately the same AGL altitude of the SBJ over the site near the base of the Sierra. The results from these studies are very revealing, but limited in horizontal context because of the type of observations employed. Wind profiles derived from rawinsondes, aircraft soundings, 915-MHz profiling Doppler radars, a scanning C-band Doppler radar[1] and combinations thereof were the primary data sources for most of these studies. Although this approach can deliver detailed vertical structure, it only provides one-dimensional information over a given horizontal location or averaging domain. Flight level data from aircraft transects across the Sierra windward slope were also employed in an attempt to document SBJ structural details (Parish 1982; Marwitz 1987), although the analyses presented in those studies were based mainly on creative inference given the sparse nature of the data that was actually collected. Finally, vertical cross sections of single Doppler radar data documented cross-barrier and along-barrier airflow associated with the SBJ from the base of the Sierra up the windward slope almost to the crest (Marwitz 1983, 1987). Unfortunately, these analyses were restricted to a single windward-slope cross section directed normal to the Sierra crest. As a result, SBJ structures west of the Sierra into the Central Valley were not revealed nor were SBJ structures along other portions of the Sierra.

As the foregoing discussion highlights, there are many questions about SBJ structural details that remain unanswered, which contributes to a deficit in knowledge about the impact of SBJs on winter storms making landfall in northern California. In particular, an incomplete

[1] Derived using the velocity–azimuth display (VAD) technique of Browning and Wexler (1968).

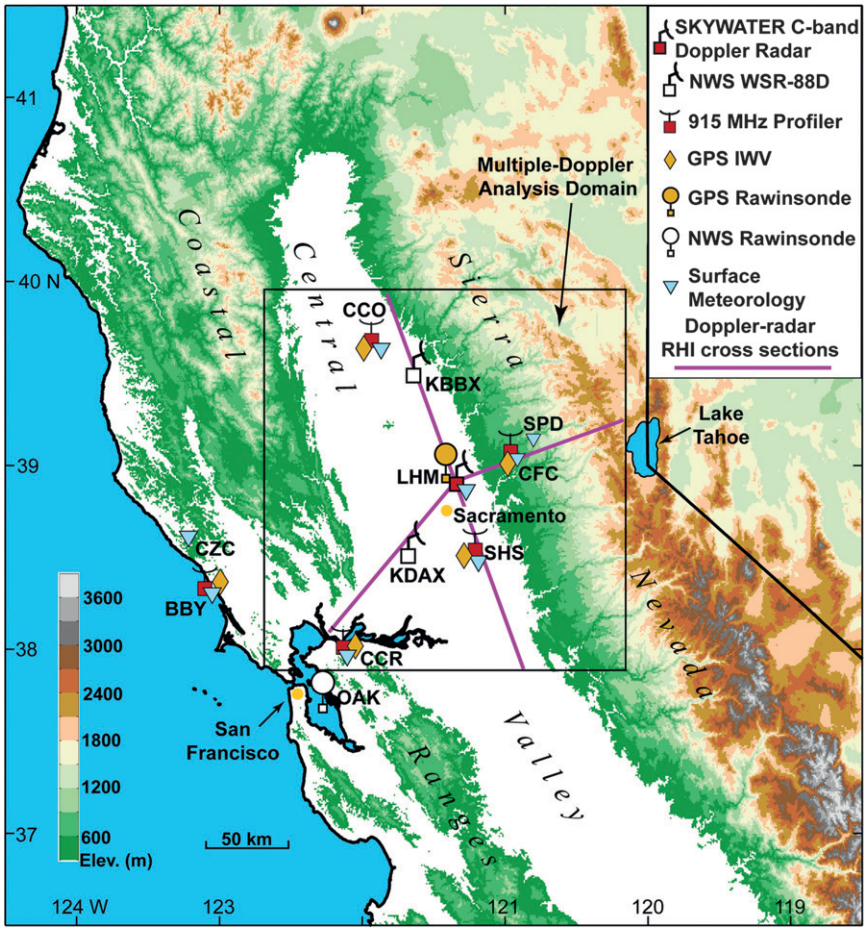

FIG. 1. HMT-West and CalWater observing systems overlaid on topographic map of northern California. Legend for the observing systems shown at the top right and color scale for terrain height is shown at the bottom left. The black rectangle centered on LHM indicates the multiple-Doppler analysis domain and the magenta line segments indicate the location of RHI cross sections from the Skywater Doppler radar.

understanding of the physics of and joint interactions between SBJs and ARs limits our ability to identify and predict the factors affecting the distribution and intensity of precipitation in California's Central Valley and along the Sierra windward slope. The present study addresses these issues with data collected from the National Oceanic and Atmospheric Administration (NOAA) Hydrometeorology Testbed (Ralph et al. 2005b; http://hmt.noaa.gov/) and the California Energy Commission CalWater project (http://www.esrl.noaa.gov/psd/calwater/) over the period 14–16 February 2011 when a strong winter storm made landfall in northern California. Detailed documentation of SBJs, ARs, and precipitation observed during this event was facilitated by a suite of scanning and profiling Doppler radars, rawinsondes, and GPS receivers. This study is unique because it characterizes the kinematic and thermodynamic structures of SBJs, landfalling ARs, and their interaction across the Central Valley and up the windward Sierra slope to the crest along an ~200-km segment of the Sierra in northern California.

2. Observing systems and data processing

Locations of the observing systems employed in this study are shown in Fig. 1. Three scanning Doppler radars were the cornerstone assets as they provided reflectivity and radial velocity data over a large portion of northern California. The NOAA/Earth System Research Laboratory (ESRL) deployed a C-band scanning Doppler radar called Skywater (Table 1) at Lincoln Regional Airport (LHM). Skywater is an upgraded Doppler version of a radar deployed in the same area during SCPP. The other two scanning radars were the National Weather Service (NWS) Weather Surveillance

TABLE 1. Characteristics of the NOAA/ESRL Skywater C-band scanning Doppler radar.

Wavelength	5.4 cm
Antenna beamwidth	1°
Peak power	250 kW
Pulse repetition frequency	1250 Hz
Pulse length	1 μs
Samples per beam	64
Gate spacing	150 m
Max unambiguous range	120 km
Nyquist velocity	16.9 m s^{-1}

Radar-1988 Doppler (WSR-88D) systems (Crum et al. 1993) located in the Central Valley near Davis (KDAX) and Oroville (KBBX). KDAX and KBBX executed volume coverage pattern (VCP) 12, a scan strategy that involves 360° surveillance scans at 14 different elevation angles between 0.5° and 19.5°, with finer vertical resolution at lower levels (Brown et al. 2005). VCP 12 repeats every ~4.5 min. Skywater also executed 360° surveillance scans and used the set of elevation angles associated with VCP 12, but restricted its scanning to elevation angles of <10°. In addition, Skywater executed 90° range–height indicator (RHI) scans at four different azimuthal angles: 70°, 160°, 220°, and 340°. The 160° and 340° RHIs are oriented parallel to the Sierra crest, the 70° RHIs are oriented perpendicular to the Sierra crest, and the 220° RHIs are parallel to the most common orientation of landfalling ARs (Neiman et al. 2008). Skywater repeated a set of three surveillance scan volumes and the four RHIs in about 13.5 min, which is approximately the same time required to complete three cycles of VCP 12 by KDAX and KBBX.

Surveillance-scan volumes from the three radars were combined to derive three-dimensional winds over the multiple-Doppler analysis domain shown in Fig. 1. The single-Doppler data were first edited to remove ground clutter and noise and to dealias folded radial velocities. These edited data were then interpolated to a 1.5 km × 1.5 km × 0.75 km Cartesian grid using an exponential distance-dependent weighting scheme, where the first analysis level was at 0.75 km MSL. Based on the criteria established by Carbone et al. (1985), the minimum resolvable horizontal wavelength with these data was 9 km. After interpolation, air motions were derived with an overdetermined dual-Doppler analysis (Kessinger et al. 1987). These wind fields were only derived when the surveillance-scan volumes from the three radars occurred within 60 s of each other. Initial horizontal velocity estimates were used to generate a convergence field, which was integrated upward with the anelastic continuity equation to calculate an initial vertical

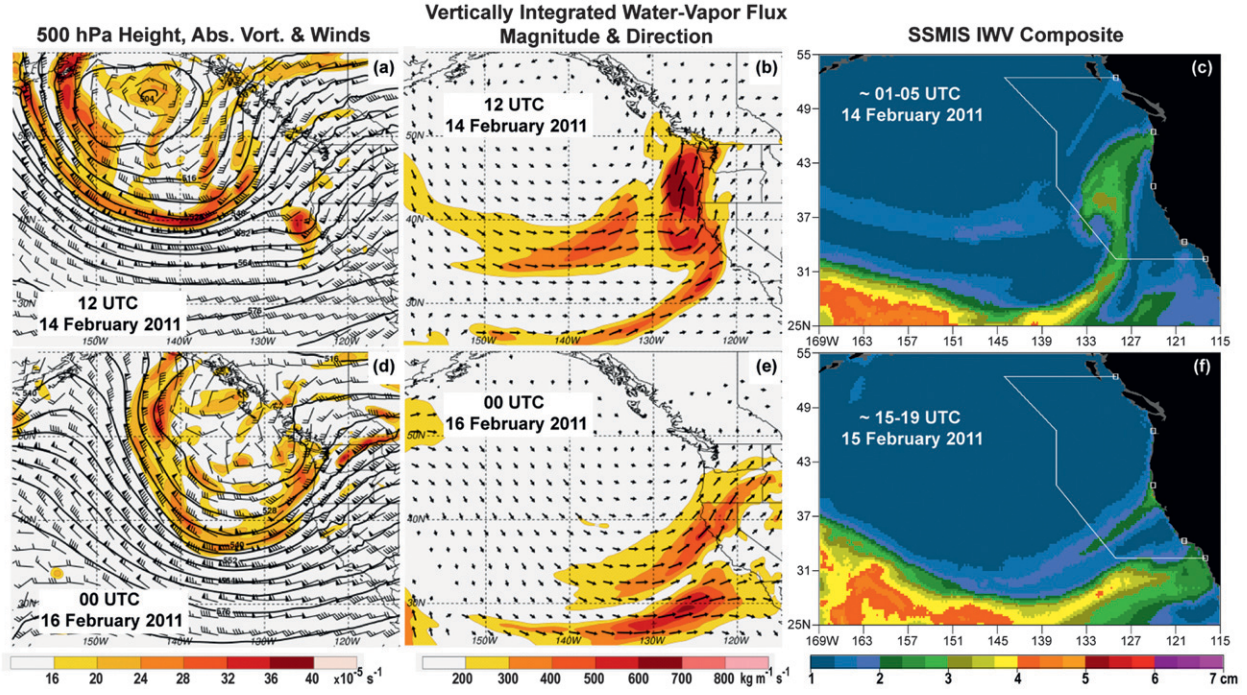

FIG. 2. (a),(d) 500-hPa height, absolute vorticity, and winds; and (b),(e) vertically integrated water vapor flux magnitude and direction from the CFSR at (a),(b) 1200 UTC 14 Feb and (d),(e) 0000 UTC 16 Feb. SSM/IS composites of retrieved IWV over the periods (c) 0100–0500 UTC 14 Feb and (f) 1500–1900 UTC 15 Feb. For the winds in (a) and (d), flags equal 25 m s^{-1}, barbs equal 5 m s^{-1}, and half-barbs equal 2.5 m s^{-1}.

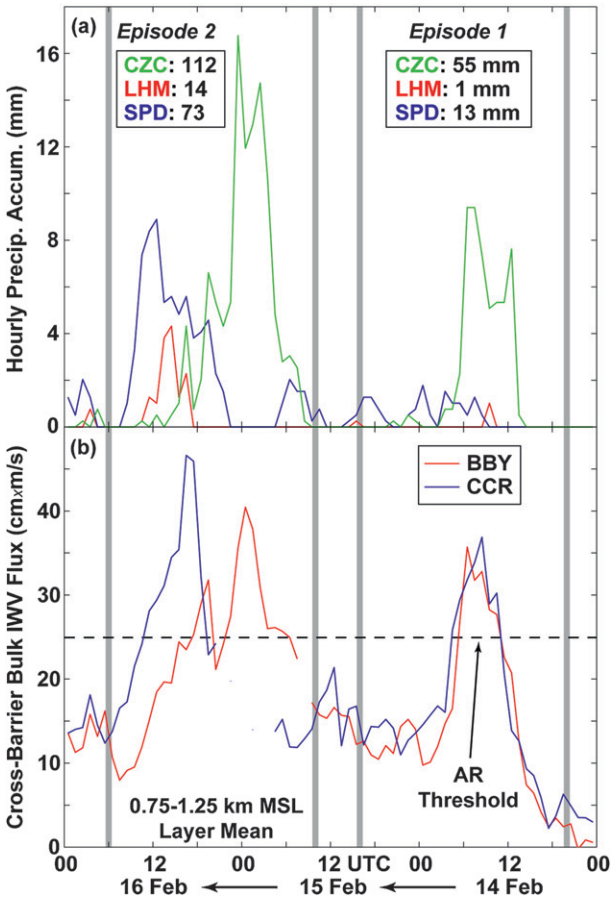

FIG. 3. Time series of regional precipitation, wind profiler, and GPS IWV observations during the event: (a) hourly precipitation accumulation at CZC (green), LHM (red), and SPD (blue); (b) hourly cross-barrier bulk IWV flux averaged over the 0.75–1.25 km MSL layer from the 915-MHz wind profilers and GPS receivers at BBY (red) and CCR (blue). Time increases from right to left to portray the advection of synoptic features from west to east. Bounds of episode 1 and 2 are indicated by the thick gray vertical lines. Total precipitation accumulations for each episode are indicated for each site in (a). Threshold for AR conditions is indicated by the dashed black line in (b).

velocity field. The integration employed a boundary condition of 0.0 m s^{-1} applied at the ground. Hydrometeor fall speeds were not incorporated into the analysis because of the relatively low elevation angles used by the contributing Doppler radars. The initial vertical velocity estimates were then used to generate a new horizontal velocity field. This procedure was repeated iteratively 2–3 times until convergence to a final solution was achieved. At that point, horizontal velocities were filtered using a two-step Leise filter (Leise 1982), which considerably damps waves less than 9 km and eliminates those less than 6 km. Uncertainties in the multiple-Doppler synthesis of horizontal velocity are estimated to be 1–2 m s^{-1} and greater than 2 m s^{-1} for vertical velocity. Since the anticipated absolute values of vertical velocity are comparable with the estimated measurement error, vertical motions are not examined in this study.

Edited surveillance scan volumes were also employed to derive VAD (Browning and Wexler 1968) vertical profiles of horizontal wind centered on each scanning radar. Annular ''rings'' of data, one range-gate wide at ranges from 5 to 30 km, were used to make a horizontal velocity estimate as long as data existed in ≥60% of the ring. All of these estimates were interpolated to a vertical grid with spacing of 100 m.

Edited Skywater RHI scans were combined to form extended cross sections of cross-barrier and along-barrier precipitation structure and airflow. As indicated by the magenta lines in Fig. 1, the 340° and 160° RHIs were merged to form an along-barrier cross section, while the 220° and 70° RHIs were merged to form a cross-barrier cross section. The horizontal component of radial velocity in the plane of each cross section was calculated except at elevation angles greater than 30°. In the along-barrier cross section, the component of horizontal flow is toward 340° (U_{340}). In the cross-barrier section, the component of horizontal flow is toward 40° (U_{40}) southwest of LHM and toward 70° (U_{70}) northeast of LHM.

Several other important observing systems contributed to the analysis. Five 915-MHz wind profiling radars (Carter et al. 1995) provided hourly averaged profiles of horizontal wind velocity (Weber et al. 1993) from ~0.1 to 4.0 km above ground, with ~100-m vertical resolution. ESRL deployed these radars along the coast at Bodega Bay (BBY), in the gap between the coastal mountains at Concord (CCR), in the Central Valley at both Sloughhouse (SHS) and Chico (CCO) and in the Sierra foothills at Colfax (CFC). Dual-frequency GPS receivers were also deployed at each of these sites, allowing retrievals of column-integrated water vapor (IWV) at 30-min intervals (e.g., Duan et al. 1996; Wolfe and Gutman 2000). In situ vertical profiles of kinematic and thermodynamic properties were provided by two rawinsonde systems: one near the coast at Oakland (OAK) operated by the NWS and another GPS-based system at LHM operated by ESRL. OAK soundings occurred at 6–12-h intervals during the event and LHM soundings occurred at 4–6-h intervals. Finally, 2-min resolution surface observations of standard meteorological parameters (i.e., temperature, relative humidity, pressure, wind, and precipitation) were collected by ESRL in the coastal mountains at Cazadero (CZC), along the west slope of the Sierra at Sugar Pine Dam (SPD) and at each of the aforementioned ESRL sites.

3. Event overview

The landfalling winter storm investigated in this study is grouped into two key periods: from 0400 UTC 14 February to 0800 UTC 15 February (i.e., episode 1) and from 1400 UTC 15 February to 1800 UTC 16 February (i.e., episode 2). Analyses from the Climate Forecast System Reanalysis (CFSR; Saha et al. 2010) and IWV retrievals (Wentz 1995) from the Special Sensor Microwave Imager/Sounder (SSMIS) polar-orbiting satellites provide synoptic-scale context for both episodes. During episode 1 (Figs. 2a–c), a broad cyclonic circulation at 500 hPa covered the Gulf of Alaska and southwesterly flow impacted the U.S. West Coast. A transient shortwave trough embedded in the southwesterly flow was making landfall across northern California at 1200 UTC 14 February and was the first significant disturbance to affect the state in several weeks. It was accompanied by a comma head of enhanced vertically integrated water vapor transport (IVT) in the layer between 1000 and 300 hPa [see Neiman et al. (2008) for calculation methodology] and a long, narrow tail of enhanced IVT characteristic of an AR extending southwestward from the central California coast. IWV satellite imagery possessed similar comma-head and comma-tail characteristics, although the IWV signatures were displaced westward relative to their IVT counterparts because the imagery was valid 7–11 h earlier. West of the landfalling AR, a second, west–east-oriented region of enhanced IVT associated with a second AR coincided with a coherent, albeit weak, band of IWV (1.33–2.0 cm) at the southern base of the broad cyclonic circulation. By 0000 UTC 16 February (Figs. 2d–f), this second AR was making landfall in northern California during the eastward migration of the parent Gulf of Alaska cyclone. This feature is associated with episode 2. The IWV within the second AR increased to >2 cm and became oriented southwest–northeast prior to landfall. The southwesterly 500-hPa flow over California was ~5 m s^{-1} stronger, and veered ~10°–15° during episode 2. Farther south, the AR with episode 1 strengthened from 36 h earlier but no longer affected northern California.

Time series of precipitation, wind profiler, and GPS-IWV observations (Fig. 3) highlight relevant meteorological characteristics in northern California during episodes 1 and 2. Hourly rainfall (Fig. 3a) at key locations in the coastal mountains (CZC), the Central Valley (LHM), and the Sierra foothills (SPD) exhibit decidedly different attributes. The coastal mountain site at CZC received 55 and 112 mm during the two episodes. In contrast, only 1 and 14 mm of rain fell at LHM in the Central Valley during episodes 1 and 2, respectively, while the rain gauge at SPD in the Sierra foothills recorded 13 and 73 mm, respectively. The prolonged dry conditions that preceded the periods of active weather likely contributed to the scant rainfall at the inland sites during the passage of the weak shortwave trough with episode 1. Because this trough moistened the atmosphere in the Central Valley, and given that the dynamics with episode 2 were stronger, there was more precipitation at LHM during the latter episode. Time series from the nearby wind profilers and GPS receivers at BBY (upwind of CZC) and CCR (upwind of LHM and SPD) exhibit comparable characteristics. The cross-barrier bulk IWV flux[2] (Fig. 3b) reveals two maxima that exceed the 25 cm m s^{-1} minimum threshold for AR conditions (Neiman et al. 2009), one during each episode. The timing of the first maximum is nearly identical at the two sites, since the axis of the transient shortwave trough aloft was oriented northwest–southeast. In contrast, the second maximum exhibits a multihour offset due to the southeastward propagation of a cold front across the domain.

A set of 14 serial rawinsondes released from LHM between 2341 UTC 13 February and 1906 UTC 16 February provides an account of the thermodynamics and kinematics in the northern Central Valley during episodes 1 and 2 (Fig. 4). A time–height section of potential temperature θ and wind profiles (Fig. 4a) shows deep tropospheric cooling and southerly component flow with the approach of the transient shortwave trough at the onset of episode 1. Terrain-trapped southerly flow persisted below ~750 hPa in a stably stratified environment for the duration of this episode, while the flow above ~700 hPa veered to west-southwesterly after ~1200 UTC 14 February following the midtropospheric trough passage. The post-trough environment did not exhibit sloping baroclinic structure below ~500 hPa. A companion time–height section of water vapor fluxes, disaggregated into the components along (toward 340°) and across (toward 70°) the Sierra Nevada, is shown in Fig. 4b. The along-barrier vapor fluxes during episode 1 were maximized (~20–60 kg s^{-1} m^{-1}) at or below 850 hPa in a shallow layer of terrain-blocked southeasterly flow. During this period, the component of the flux oriented perpendicular to the Sierra attained its largest value (~40 kg s^{-1} m^{-1}) in southwesterly flow at ~800 hPa immediately following passage of the

[2] The cross-barrier IWV flux is defined as the product of the cross-barrier wind speed orthogonal to the Sierra (U_{70}) measured hourly by the BBY and CCR wind profilers in the layer between 0.75 and 1.25 km MSL and the hourly IWV measured concurrently at the same sites (e.g., Neiman et al. 2009). Because water vapor is typically concentrated in the lower troposphere, the IWV flux is a first-order estimate of low-level water vapor flux.

shortwave trough axis. The along-barrier component of vertically integrated (1000–150 hPa) water vapor flux (IVT) slightly exceeds its cross-barrier counterpart throughout episode 1 (Fig. 4c).

The time–height section of θ (Fig. 4a) documents an intensification of a capping stable layer at ~725 hPa at the onset of episode 2. This lamina was situated beneath the Sierra crest and separated weakly stratified southerly flow below from stable southwesterly flow aloft. Later in the episode, deep tropospheric cooling and a wind shift from southerly component to westerly component marked the passage of a well-defined cold front during the landfall of the synoptic-scale cyclone. Shallow along-barrier vapor fluxes persisted during episode 2 (Fig. 4b), terminating with the passage of the cold front. Immediately prior to frontal passage, the top of this terrain-parallel flux corridor increased significantly in altitude as a result of a deepening layer of strengthening, prefrontal south-southwesterly flow. The intensification of the prefrontal flow also contributed to a local maximum of terrain-perpendicular vapor fluxes centered at ~700 hPa. Along-barrier IVT remained slightly larger than cross-barrier IVT during episode 2 until the cold-frontal passage when the latter decreased less rapidly than the former (Fig. 4c).

4. Detailed structure of the SBJ and AR

a. Episode 1

A time–height section of winds at the SHS profiler shows the largest cross-barrier wind speeds U_{70} between ~1200 and 1800 UTC 14 February above 1.5 km (Fig. 5). Maximum values exceed 20 m s^{-1} from the southwest. This airflow is associated with the AR. The largest along-barrier wind speeds U_{340} are first evident above 1.5 km MSL prior to 1200 UTC 14 February. Maximum values of U_{340} descend with time to below 1.5 km MSL and strengthen to >24 m s^{-1} in the terrain-parallel south-southeasterly flow between ~1600 and 2100 UTC. The initial, elevated U_{340} maximum can be attributed mostly to enhanced meridional flow associated with the leading edge of the shortwave trough (Fig. 2a) and is probably not a barrier-induced feature. In contrast, the second maximum at low levels is characteristic of a SBJ (Neiman et al. 2010). After 0000 UTC 15 February, both cross- and along-barrier wind speeds decrease significantly, and no frontal passage is evident in the wake of the shortwave trough.

Figure 6 provides an analysis of radar reflectivity and horizontal winds over the multiple-Doppler domain at 1800 UTC 14 February when the SBJ magnitude was maximized at SHS during episode 1. The reflectivity fields show scattered 20–40 dBZ_e echoes superimposed on widespread weak echoes of <10 dBZ_e. This pattern is consistent with the relatively limited amount of precipitation observed in the Central Valley and along the windward Sierra slope during episode 1. The coverage of synthesized horizontal winds is somewhat restricted relative to reflectivity due to both the scattered reflectivity pattern and geometrical constraints associated with the multiple-Doppler analysis. The limited coverage is particularly evident at the lowest analysis level (Figs. 6j–l) because the lowest elevation-angle surveillance scan (0.5°) passed above the 0.75 km MSL level at a range of ~60 km. Horizontal winds are generally from the south-southeast at low levels, veering to southwesterly as height increases (Figs. 6a,d,g,j), which is also illustrated in the plots of U_{70} and U_{340} (Figs. 6b,c,e,f,h,i,k,l). On average, U_{70} increases with height and U_{340} decreases with height. Larger U_{70} at 1.5, 2.25, and 3 km (15–25 m s^{-1}) is associated with the synoptically driven southwesterly flow linked to the AR, while larger U_{340} at 0.75, 1.5, and 2.25 km (15–25 m s^{-1}) is likely associated with the SBJ. Both of these features are relatively broad and diffuse and exhibit considerable variability across the domain.

RHI scans from Skywater are used to create a cross-barrier vertical cross section of reflectivity and horizontal airflow at 1803 UTC. The cross-barrier vertical cross section is positioned along the A-LHM-B line segments shown in Figs. 6b,e,h,k. Reflectivity along this cross section is cellular (Fig. 7a), consistent with the structure observed in the multiple-Doppler analysis. Echo tops only extend up to 2–3 km MSL southwest of LHM in the Central Valley but rise to ~4 km MSL over and northeast of LHM. Although reflectivity values increase below the LHM 0°C level, a distinct brightband signature is not evident.

Horizontal winds along the plane of this cross section indicate a layer of enhanced vertical shear that slopes upward from southwest to northeast (Fig. 7b), with larger values of U_{40} and U_{70} above smaller values. The shear layer extends ~100 km southwest of LHM at the western edge of the Central Valley near the gap in coastal terrain northeast of San Francisco, California, and ~75 km northeast of LHM along the upper windward Sierra slope. A discontinuity in wind speed exists at LHM due to the transition from U_{40} to U_{70} at the intersection of the two RHI scans. However, the shear layer remains continuous across this interface. At its southwest edge, the level of maximum shear rises abruptly from the surface to ~1.2 km and is coincident with enhanced reflectivity. Moving northeast, the maximum-shear level descends slightly to ~0.8 km MSL and then starts to gradually increase in altitude at a rate of ~1% as it

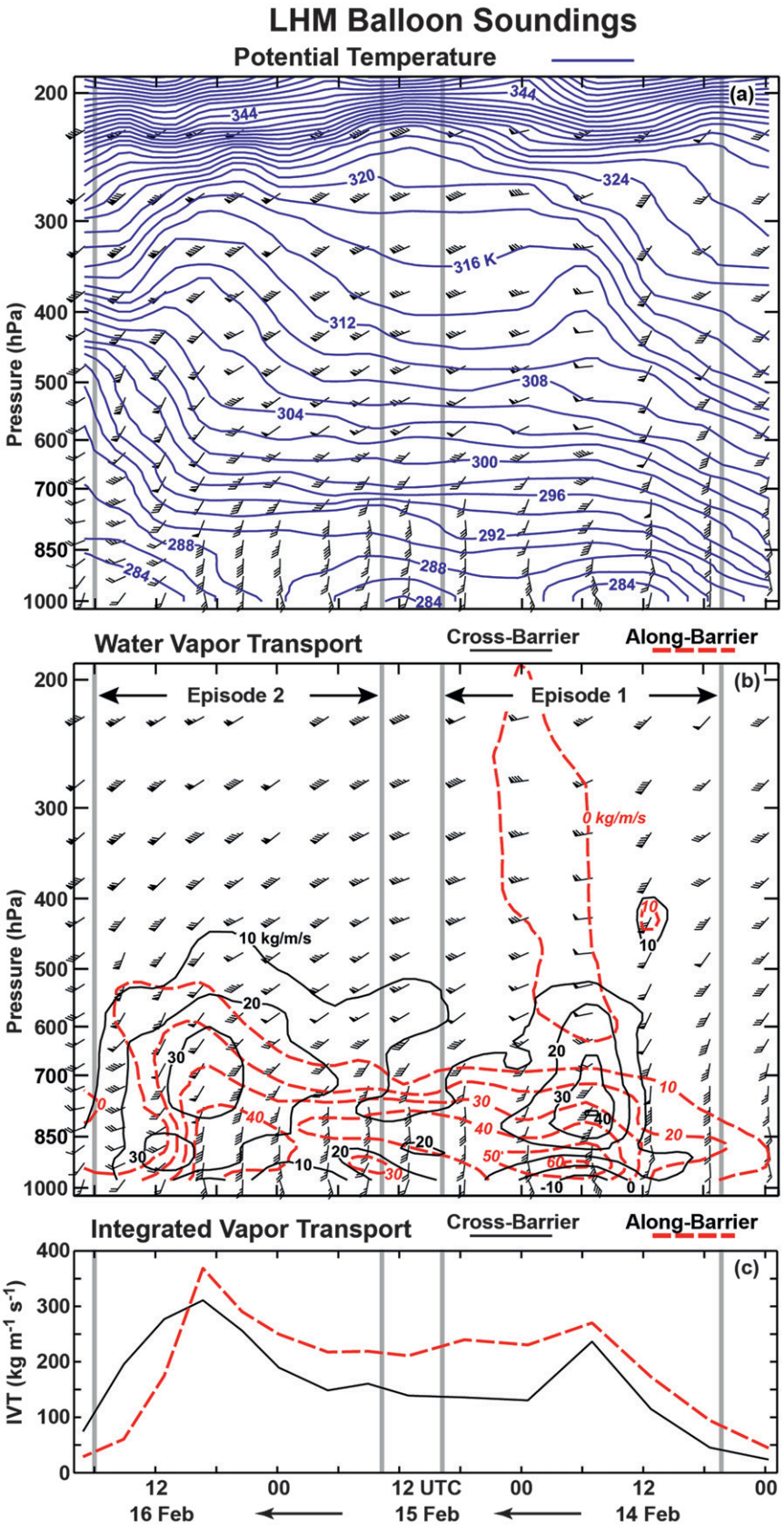
LHM Balloon Soundings
Potential Temperature
(a)
Pressure (hPa)
200
300
400
500
600
700
850
1000
344
320
324
316 K
312
308
304
300
296
292
288
284
Water Vapor Transport
Cross-Barrier
Along-Barrier
(b)
Episode 2
Episode 1
0 kg/m/s
10 kg/m/s
Integrated Vapor Transport
(c)
IVT (kg m-1 s-1)
0
100
200
300
400
12
00
12 UTC
16 Feb
15 Feb
14 Feb

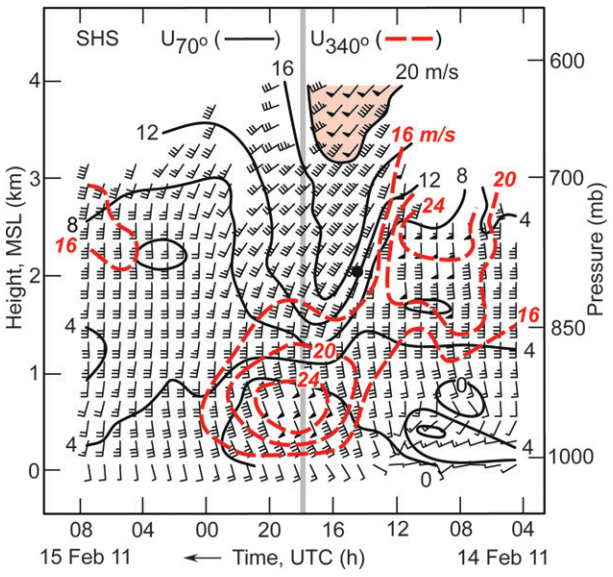

FIG. 5. Time–height cross section of hourly winds from the 915-MHz wind profiler at SHS during episode 1. Flags and barbs are as in Fig. 4. Time increases from right to left to portray the advection of synoptic features from west to east. Contours of cross-barrier U_{70} and along-barrier U_{340} wind speed are shown by the black solid and red dashed lines, respectively. Values of U_{70} greater than 20 m s^{-1} are filled with light red. Estimates of snow level are indicated by black-filled circles. The time of a multiple-Doppler analysis shown in Fig. 6 is indicated by a thick gray vertical line.

approaches LHM. Northeast of LHM the level of maximum shear increases its rate of ascent to almost 2% and rises to ~2 km MSL.

The relatively strong U_{40} and U_{70} above the shear layer are likely linked to the comparably oriented AR. In contrast, much weaker to slightly negative U_{40} and U_{70} within and below the shear layer correspond to the SBJ. The latter assertion requires more documentation, which is provided by profiles of U_{40}, U_{70}, and U_{340} derived from the 915-MHz wind profilers at CCR and CFC between 1700 and 1900 UTC and from VAD analyses at KDAX and LHM at ~1800 UTC (Figs. 7c–f). Profiles of U_{40} at KDAX and U_{70} at CFC are similar to profiles of U_{40} and U_{70} inferred from the RHI over those sites (Fig. 7b), which provides an independent measure of consistency between these different datasets. Upstream of the shear layer at CCR, the profiles of U_{40}, U_{70}, and U_{340} have a relatively similar shape in the lowest 2 km. All three profiles have maximum values at ~1 km MSL, with U_{40} being the largest at ~21 m s^{-1}. Wind directions in this layer range from 195° to 210° (not shown), consistent with the low-level jet associated with an AR. However, profiles at KDAX, LHM, and CFC are fundamentally different. Maximum values of U_{340} in excess of 20 m s^{-1} are evident at the lowest analysis level (~0.3 km MSL) over KDAX, at ~0.8 km MSL over LHM and at ~1.5 km MSL over CFC. These terrain-parallel maxima occur in the context of cross-barrier airflow (U_{40} and U_{70}) that minimizes at the lowest analysis level and increases with height through and above the terrain-parallel maxima (i.e., the cross-barrier shear layer). This is a structure characteristic of the SBJ, which supports the assertion that the SBJ corresponds to the weak and slightly negative cross-barrier horizontal airflow within and below the shear layer as illustrated in the RHI (Fig. 7b).

To assess the impact of terrain on horizontal airflow, the observed winds are compared against geostrophic winds derived from the CFSR. Average CFSR geostrophic values of U_{40}, U_{70}, and U_{340} are calculated within the multiple-Doppler analysis domain west of the C-D line segment shown in Figs. 6c,f,i,l. In the multiple-Doppler analysis, observed U_{70} is generally smaller than geostrophic U_{70} (Figs. 6b,e,h,k), while observed U_{340} is generally larger than its geostrophic counterpart (Figs. 6c,f,i,l). These departures from geostrophy are largest at the lowest analysis level and decrease with height up to 2.7 km, the approximate altitude of the Sierra crest in the analysis domain. A similar pattern is evident when comparing profiles of U_{40}, U_{70}, and U_{340} at KDAX (Fig. 7d), LHM (Fig. 7e), CFC (Fig. 7f), and, to a lesser extent, CCR (Fig. 7c) with profiles of CFSR geostrophic U_{40}, U_{70}, and U_{340} (Fig. 7g). These trends are indicative of ageostrophic motions associated with a cross-barrier airstream blocked by the Sierra and deflected leftward in an along-barrier direction.

←

FIG. 4. Time–height cross section of winds, (a) potential temperature, and (b) water vapor transport from 14 rawinsondes released at LHM. Time increases from right to left to portray the advection of synoptic features from west to east. For the winds: flags equal 25 m s^{-1}, barbs equal 5 m s^{-1}, and half-barbs equal 2.5 m s^{-1}. In (b), water vapor transport is separated into cross-barrier (toward 70° azimuth) and along-barrier (toward 340° azimuth) components, shown by the black solid and red dashed lines, respectively. (c) IVT from 1000–150 hPa for both cross-barrier and along-barrier components is shown. Bounds of episodes 1 and 2 are indicated by the thick gray vertical lines.

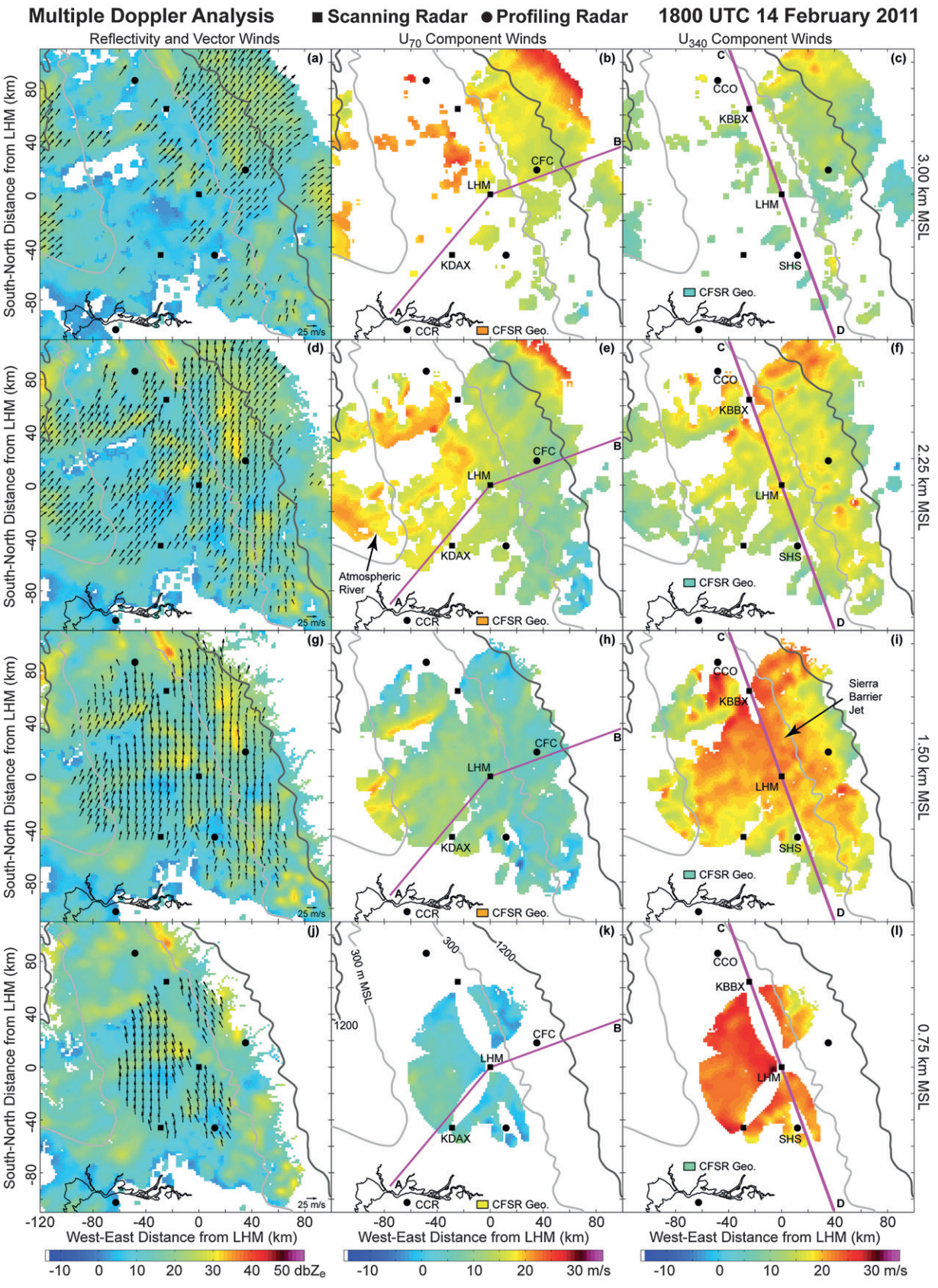
Multiple Doppler Analysis
Scanning Radar
Profiling Radar
1800 UTC 14 February 2011
Reflectivity and Vector Winds
U70 Component Winds
U340 Component Winds
South-North Distance from LHM (km)
West-East Distance from LHM (km)
3.00 km MSL
2.25 km MSL
1.50 km MSL
0.75 km MSL
CCO
KBBX
CFC
LHM
KDAX
SHS
CCR
CFSR Geo.
Atmospheric River
Sierra Barrier Jet
300 m MSL
300
1200
25 m/s
-10 0 10 20 30 40 50 dbZe
-10 0 10 20 30 m/s

During this period of blocked flow, static stability is characterized with a rawinsonde released from LHM at 1702 UTC 14 February (Fig. 8). A rawinsonde from OAK at 1800 UTC is also shown in Fig. 8 to provide a reference for conditions upstream of the Central Valley. The profile of θ from both soundings increases in the lowest 3 km, with the rate of increase somewhat larger at LHM (Fig. 8a). Dry and saturated Brunt–Väisälä frequency squared (N^2 and N_m^2, respectively; Durran and Klemp 1982) within this layer indicates generally stably stratified conditions at both locations, with noticeably stronger static stability over LHM in the 0.5–1.2-km layer (Figs. 8b,c). Below ~1 km MSL, the stability was nearly neutral to weakly unstable for N_m^2 (especially at OAK), although the relative humidity in this layer was unsaturated (i.e., <90%), which makes N^2 most applicable.

Static stability is a necessary but insufficient condition for terrain blocking to occur. Rather, the nondimensional Froude number must be greater than zero but less than one. Froude number (Fr) for this application is defined as U_{70}/Nh where U_{70} is the upstream cross-barrier wind speed for the Sierra, N is the Brunt–Väisälä frequency, and h is the Sierra crest altitude (~2.7 km). Saturated Froude number (Fr_m) employs N_m instead of N. The U_{70} profile from OAK was used in the calculation of Froude numbers for both soundings since U_{70} from LHM is not an upstream profile and shows negative values in the lowest 1 km (Fig. 8d), a signature likely attributed to Sierra blocking. The OAK U_{70} profile also has slightly negative values in the lowest 0.3 km, but those are most likely caused by local terrain effects and not by the Sierra. Froude numbers Fr and Fr_m are not derived at levels where $N_m^2 \leq 0$ and $U_{70} \leq 0$.

The Fr increases with height in the lowest 1.5 km to a value of ~0.5 for both rawinsondes (Fig. 8e). Values of Fr_m (Fig. 8f) are mostly less than or equal to 1 in the layers of both soundings with relative humidity greater than 90%. LHM Fr_m is generally smaller than OAK Fr_m below 1.7 km. These profiles of Froude number along with the earlier described profiles of squared Brunt–Väisälä frequency suggest that blocking is a likely explanation for the observed ageostrophic airflow patterns observed in the lowest 3 km. However, they do not provide guidance on the upstream extent of blocking predicted by theory. The Rossby radius of deformation L_R provides an estimate of the upstream distance that a mountain can induce blocking relative to its crest (Pierrehumbert and Wyman 1985). Here L_R is defined as Nh/f, where N is the Brunt–Väisälä frequency, h is the Sierra crest altitude (~2.7 km), and f is the Coriolis parameter. Using the 0–2.7 km MSL mean N^2 and N_m^2 from LHM in Fig. 8 yields L_R values of ~380 and ~200 km, respectively. The former extends well offshore of California while the latter extends only ~10 km southwest of the southwestern edge of the cross-barrier shear layer in Fig. 7b.

An along-barrier vertical cross section at 1807 UTC positioned along the C-LHM-D line segments shown in Figs. 6c,f,i,l allows for detailed characterization of SBJ vertical structure. As in the cross-barrier cross section, reflectivity is cellular in nature (Fig. 9a). Maximum reflectivity values occur at and below the 0°C level, but extend through an almost 1-km vertical layer that is thicker than a typical bright band. Echo tops are mainly 3–4 km MSL, except to the northwest near CCO where they are a little above 2 km MSL. Horizontal winds along the plane of this cross section indicate a low-level maximum of U_{340} (25–30 m s^{-1}) associated with the SBJ (Fig. 9b), which increases in altitude toward the northwest. The thickness of the SBJ core increases in a similar manner. An explanation for these trends is not obvious, but may be related to a southeast–northwest increase of precipitation accumulation along the Sierra (not shown). In this hypothesis, diabatic cooling associated with the precipitation from evaporating rain and melting snow is enhanced toward the northwest, allowing larger amounts of cool air to be injected into the northern Central Valley through low-level downslope flow in river valleys along the west slope of the

←

FIG. 6. Multiple-Doppler (Skywater KDAX, and KBBX) derived horizontal winds and radar reflectivity at ~1800 UTC 14 Feb within the domain shown in Fig. 1 at (a)–(c) 3 km MSL, (d)–(f) 2.25 km MSL, (g)–(i) 1.5 km MSL, and (j)–(l) 0.75 km MSL. The coordinate origin is at LHM. In (a),(d),(g),(j), wind vectors are overlaid on a reflectivity field composited from Skywater, KDAX, and KBBX by selecting the maximum value at each grid point. Reference wind vectors are indicated at the bottom right of each panel, and a color scale for reflectivity is shown at the base of the column. Cross-barrier U_{70} and along-barrier U_{340} components of horizontal wind are displayed in (b),(e),(h),(k) and (c),(f),(i),(l), respectively. Corresponding color scales are shown at the base of each column. Color-coded average geostrophic values of U_{70} and U_{340} derived from the CFSR are shown in each panel of the middle and right columns, respectively. The location of the Skywater RHI cross section shown in Fig. 7 is indicated in the middle column by magenta line segments A-LHM-B. Likewise, the Skywater RHI cross section shown in Fig. 9 is indicated in the right column by magenta line segments C-LHM-D. The locations of scanning and profiling radars are shown in all 12 panels by black squares and circles, respectively. Contours of 300 and 1200 m MSL terrain elevation are indicated by the light and dark gray lines, respectively. The positions of the AR and SBJ are indicated.

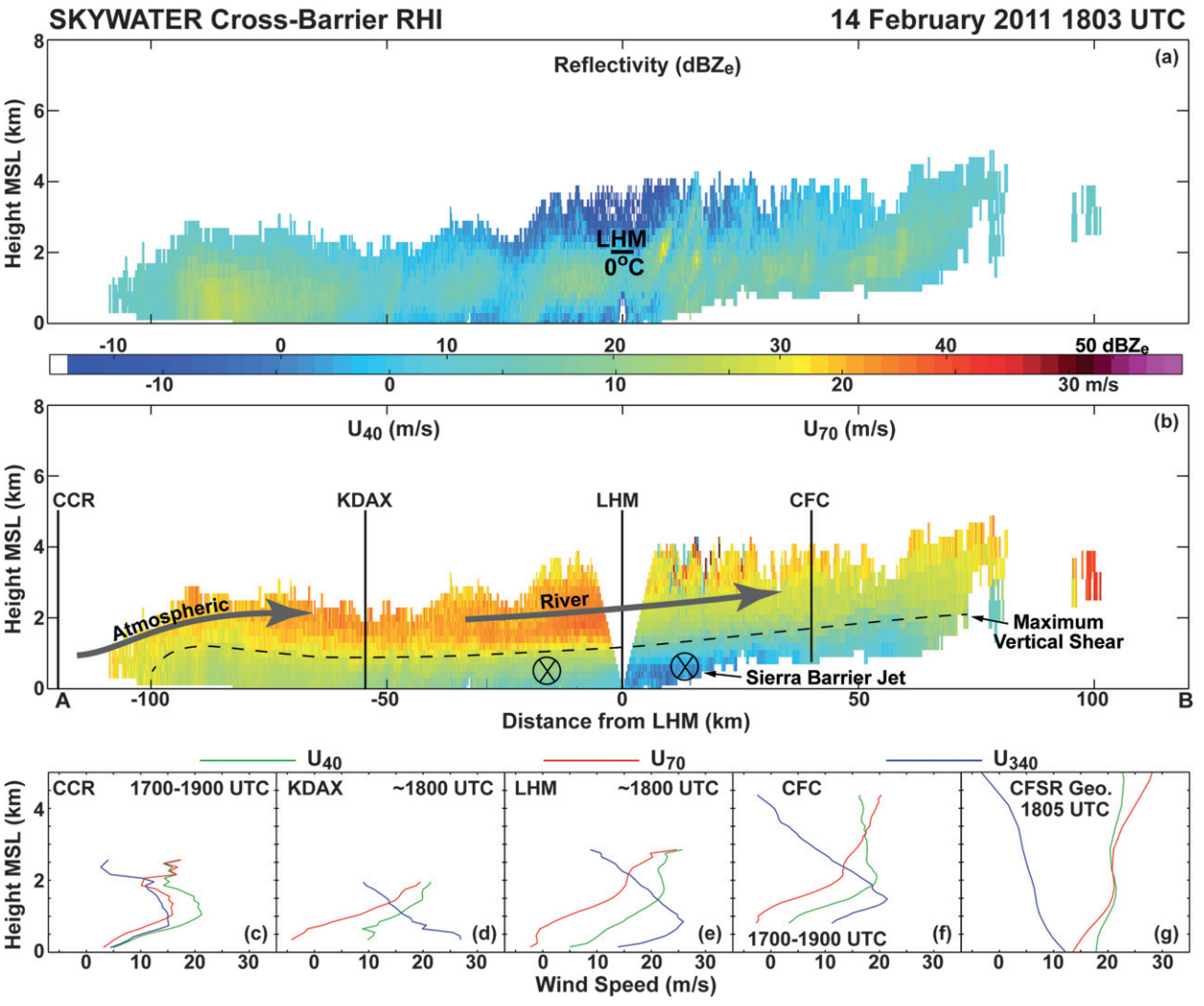

FIG. 7. Merger of 220° and 70° RHI scans from Skywater at ~1803 UTC 14 Feb to form a cross-barrier vertical cross section along the A-LHM-B line segments shown in Fig. 6. (a) Reflectivity is displayed along with the 0°C level from an LHM rawinsonde released at 1702 UTC. (b) Cross-barrier horizontal wind speed (U_{40} southwest of LHM and U_{70} northeast of LHM) is shown. A color scale for reflectivity and cross-barrier wind speed is located between (a) and (b). The positions of the AR and SBJ are indicated by thick gray arrows, and the altitude of maximum vertical shear of U_{40} and U_{70} is indicated by the thin black dashed line. Vertical black lines in (b) indicate the location of U_{40} (green), U_{70} (red), and U_{340} (blue) profiles over (c) CCR, (d) KDAX, (e) LHM, and (f) CFC. The CCR and CFC profiles are from the 915-MHz profilers at those sites and averaged over the period 1700–1900 UTC. The KDAX and LHM profiles are produced from VAD analyses of the KDAX and Skywater surveillance scans that contributed to the multiple-Doppler analysis at ~1800 UTC. (g) Profiles of CFSR geostrophic U_{40}, U_{70}, and U_{340} at 1805 UTC are shown.

Sierra (Steiner et al. 2003). This process would foster deepening of the stable air mass in the Central Valley toward the northwest.

Profiles of U_{340} at SHS, LHM, KBBX, and CCO also show the trend of increasing SBJ height from southeast to northwest (Figs. 9c–f). The corresponding trend in SBJ-layer thickness is not as clear, perhaps because at its northwest end the cross section is over the southwestward protrusion of the Sierra while CCO is located in the Central Valley about 10 km to the southwest. All profiles indicate the cross-barrier shear layer in U_{70} through and above the SBJ. Both the U_{70} and U_{340} components of horizontal motion exhibit the largest ageostrophic departures in the lowest 2–3 km, which is evident upon comparison with the geostrophic profiles of these parameters in Fig. 9g.

b. *Episode 2*

Cross-barrier wind speeds U_{70} over SHS during episode 2 (Fig. 10) are larger than those occurring during episode 1 (Fig. 5). The large values of U_{70} that extend from 1–4 km MSL during 0500–1100 UTC 16 February

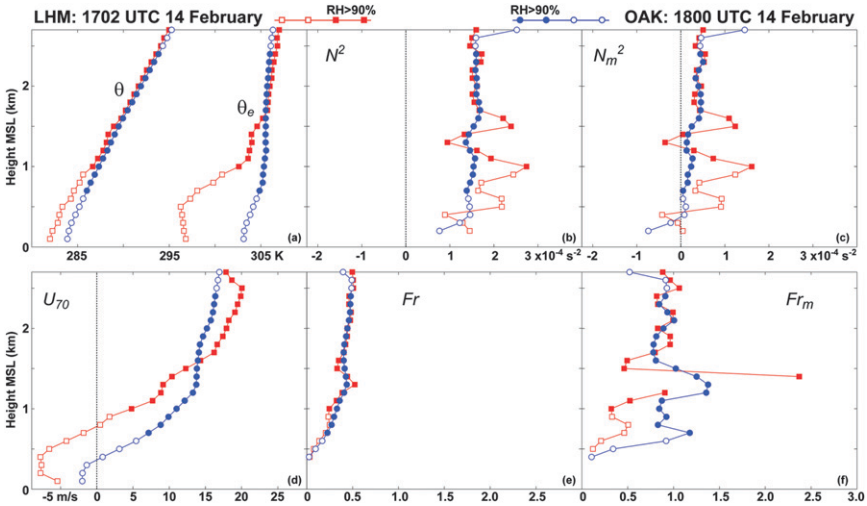

FIG. 8. Profiles of (a) potential temperature and equivalent potential temperature, (b) squared Brunt–Väisälä frequency, (c) squared moist Brunt–Väisälä frequency, (d) cross-barrier wind speed orthogonal to the Sierra, (e) Froude number, and (f) moist Froude number from rawinsondes released from LHM at 1702 UTC 14 Feb (red squares) and from OAK at 1800 UTC 14 Feb (blue circles). Native vertical resolution data from both soundings (LHM: ~5 m; OAK: ~175 m) has been interpolated to a 100-m vertical grid. Levels of the LHM and OAK profiles where relative humidity exceeds 90% have plot symbols that are filled with red and blue, respectively.

represent the pre-cold-frontal southwesterly flow associated with the second AR. The largest along-barrier wind speeds U_{340} are first observed in the 1.5–2.0 km MSL layer, initially at ~1800 UTC 15 February and then again at ~0500 UTC 16 February. An elevated maximum in U_{340} was also observed in association with episode 1 (Fig. 5). While that maximum was attributed to the leading edge of a shortwave trough, the same explanation does not apply here because of the longwave nature of the trough making landfall (Fig. 2d). The cause of these features is not clear but is likely induced by the Sierra since they are below the Sierra-crest height (~2.7 km MSL) and the same features are not observed ~100 km to the southwest at CCR (not shown). After 0500 UTC, maximum values of U_{340} descend below 1.5 km MSL and peak from about 0600 to 1000 UTC (Fig. 10). This airflow is likely associated with the SBJ. In contrast to episode 1, the low-level U_{340} maximum associated with the SBJ during episode 2 is weaker (<24 m s^{-1}), does not have an easterly component, and is coincident with the strongest U_{70} aloft. Another difference from episode 1 is the occurrence of a distinct cold-frontal passage, which is evident after 1100 UTC by a low-level wind-direction transition from southerly to westerly and a descending snow level.

Figure 11 shows radar reflectivity and horizontal winds over the multiple-Doppler domain at 0701 UTC 16 February, during the intensifying SBJ at SHS. The reflectivity field shows stronger (35–45 dBZ_e) and more widespread echoes than in episode 1, hence, coverage of synthesized horizontal winds extends over a larger volume. Across the eastern half of the domain these winds are generally from the south, but veer toward southwesterly moving westward and upward (Figs. 11a, d,g,j). These wind variations are illustrated with plots of U_{70} and U_{340} (Figs. 11b,c,e,f,h,i,k,l). The sharpest horizontal gradient in both U_{70} and U_{340} is ~40 km west of LHM and is associated with the cold front. This gradient slopes westward with increasing height, which is consistent with a westward tilt of the front. A line of enhanced reflectivity is evident along portions of the cold front. West of the cold front there are banded U_{70} maxima oriented southwest to northeast that are hypothesized to be Kelvin–Helmholtz waves atop the postfrontal air mass (e.g., Friedrich et al. 2008; Houser and Bluestein 2011). Unfortunately, the coarse vertical resolution of the multiple-Doppler analysis and the lack of Skywater RHI scans directed orthogonal to the front limit our ability to test this hypothesis. The relatively large U_{70} (15–25 m s^{-1}) immediately east of the cold front is associated with the prefrontal low-level jet and is linked to the AR. As height increases, maximum values of U_{70} increase and the area of maximum U_{70} increases, while extending farther east and north. The AR is also associated with relatively large U_{340}

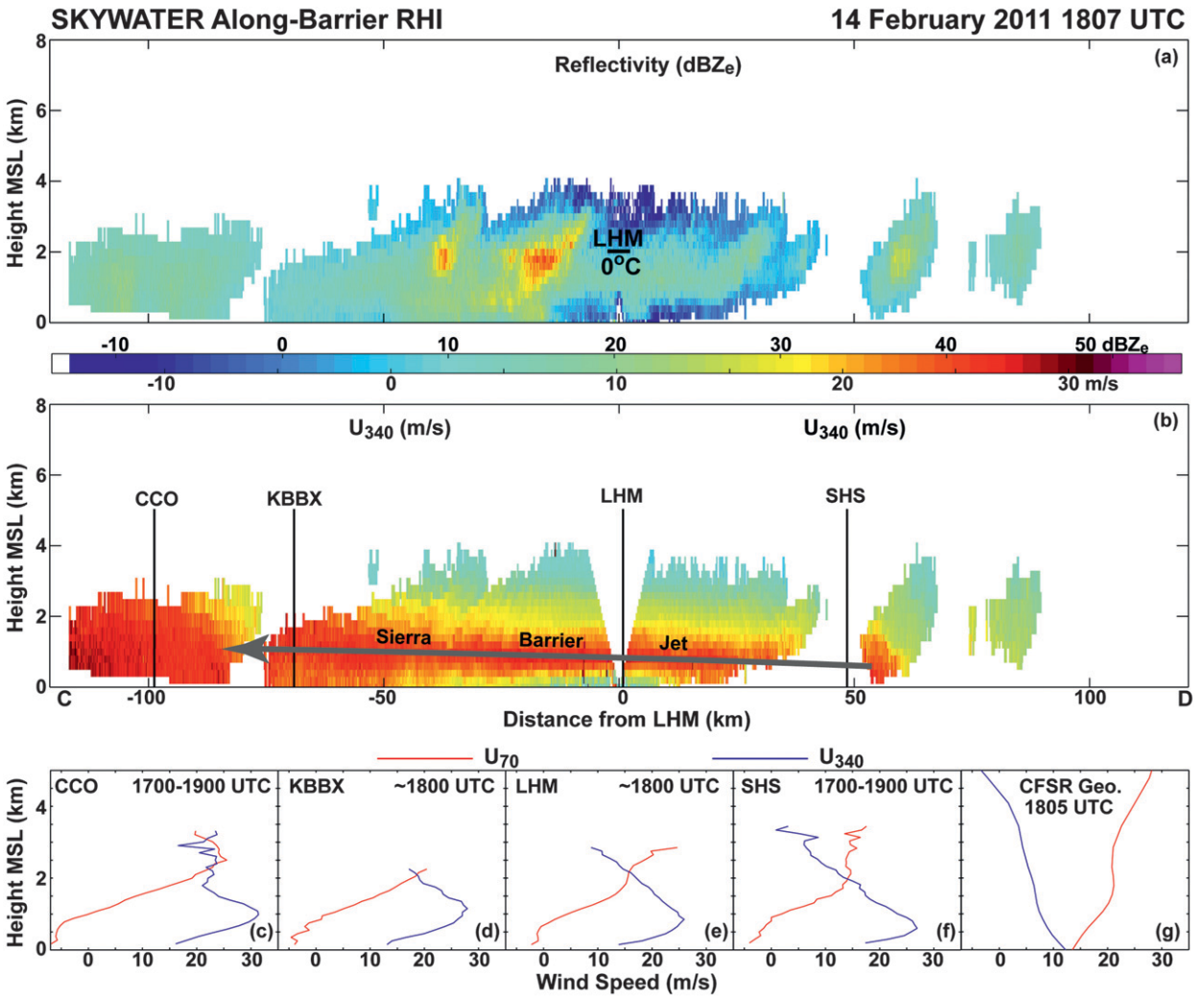

FIG. 9. Merger of 340° and 160° RHI scans from Skywater at ~1807 UTC 14 Feb to form an along-barrier vertical cross section along the C-LHM-D line segments shown in Fig. 6. (a) Reflectivity is displayed along with the 0°C level from a LHM rawinsonde released at 1702 UTC. (b) Along-barrier horizontal wind speed U_{340} is shown. A color scale for reflectivity and along-barrier wind speed is located between (a) and (b). The position of the Sierra barrier jet (SBJ) is indicated. Vertical black lines in (b) indicate the location of U_{70} (red) and U_{340} (blue) profiles over (c) CCO, (d) KBBX, (e) LHM, and (f) SHS. The CCO and SHS profiles are from the 915-MHz profilers at those sites and averaged over the period 1700–1900 UTC. The KBBX and LHM profiles are produced from VAD analyses of the KBBX and Skywater surveillance scans that contributed to the multiple-Doppler analysis at ~1800 UTC. (g) Profiles of CFSR geostrophic U_{70} and U_{340} at 1805 UTC are shown.

adjacent to the front. However, in contrast to U_{70}, maximum values of U_{340} in this area decrease with increasing height. Another focused area of large U_{340} (20–30 m s^{-1}) is located along the Sierra and tied to the SBJ. The western boundary of this area tilts eastward with height. In this area, observed U_{340} is larger than geostrophic U_{340}, and observed U_{70} is less than geostrophic U_{70}, implying that the SBJ is characterized by ageostrophic motions. The relative orientations of the U_{340} maximum associated with the SBJ and the U_{70} maximum associated with the AR suggest a merger of these features in the northern part of the domain.

The cross-barrier vertical structure of the pre-cold-frontal AR and SBJ from Skywater RHI scans at 0704 UTC is shown in Fig. 12 (along A-LHM-B in Figs. 11b,e, h,k). Not only is the reflectivity stronger compared to episode 1, the echo tops are higher, rising to 5–7 km MSL (Fig. 12a). A distinct brightband signature is evident at or slightly below the LHM 0°C level. This feature slopes downward from KDAX to CFC in a manner similar to that documented by Marwitz (1983). Minder et al. (2011) and Minder and Kingsmill (2013) have attributed this type of structure to a combination of diabatic and pseudoadiabatic processes. Similar to episode 1,

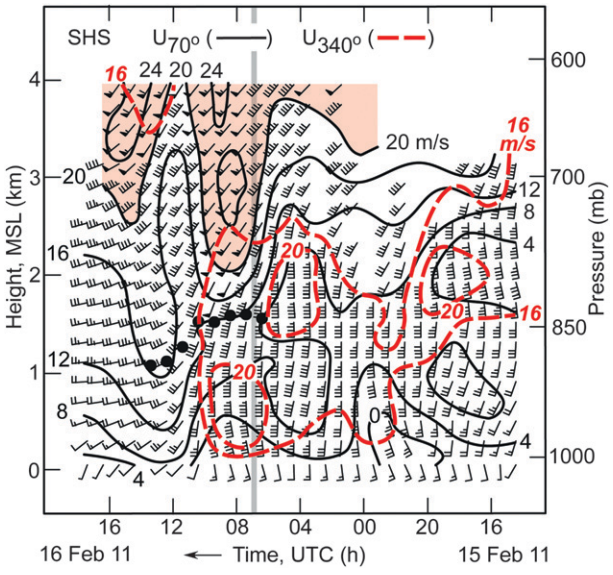

FIG. 10. As in Fig. 5, but for episode 2. The thick gray vertical line indicates the time of a multiple-Doppler analysis shown in Fig. 11.

a layer of vertical shear in U_{40} and U_{70} slopes upward from southwest to northeast (Fig. 12b). However, this shear layer only extends ~75 km southwest of LHM, ~25 km northeast of where the shear layer extended during episode 1. At its southwest edge, the level of maximum shear rises to ~1 km MSL with an average slope of ~1%. The slope increases dramatically to ~4% about 25 km southwest of LHM and continues at that rate until about 25 km northeast of LHM where the maximum shear level is centered at ~3 km MSL. Farther northeast, the axis of maximum shear continues to rise, but only at a rate of ~2%.

The strong and deep U_{40} and U_{70} above the shear layer correspond to the AR while the adjacent airflow below corresponds to the SBJ. Profiles of U_{340} at KDAX (Fig. 12d), LHM (Fig. 12e), and CFC (Fig. 12f) confirm the latter assertion. Similar to episode 1, the layer of maximum U_{340} associated with the SBJ occurs within and below the cross-barrier shear layer seen in the profiles of U_{40} and U_{70}. However, the U_{340} maxima are deeper and positioned higher. Maximum U_{340} at KDAX and LHM is ~20 m s^{-1}, ~5 m s^{-1} weaker than those observed during episode 1, while at CFC, maximum U_{340} is ~5 m s^{-1} stronger (~25 m s^{-1}). Ageostrophic motions are most evident in the lowest 2–3 km of these profiles (cf. Fig. 12g). The CCR profile (Fig. 12c) also exhibits a distinct low-level U_{340} maximum characteristic of the SBJ. However, wind directions associated with this maximum vary over a narrow range from 200° to 215° (not shown), which is more characteristic of the AR than the SBJ. Interestingly, the CCR profile indicates a cross-barrier shear layer but such a structure is not evident at the southwestern edge of the Skywater RHI (Fig. 12b), which is ~15 km northwest of CCR. This may result from the inability of Skywater to detect the relatively weak cross-barrier airflow at low levels as a result of the earth-curvature effects at long range.

Static stability associated with these airflow structures is characterized with rawinsondes from LHM at 0719 UTC and from OAK at 0600 UTC (Fig. 13). Both rawinsondes indicate a less stable environment in the lowest 1.5 km than during episode 1. OAK is dry neutral and moist unstable in the lowest 0.5 km, while LHM exhibits those same characteristics in the 0.5–1.5-km layer. This is consistent with the idea that the air mass at OAK is lifted up and over the SBJ. Absolute stability is evident in the 1.5–2.7-km layer of both rawinsondes. Froude numbers Fr and Fr_m are intermittently very large or undefined in the lowest 1.5 km because of the near-neutral or unstable stratification observed in portions of that layer over LHM and OAK. However, where dry and moist static stability exists in the profiles, Fr and Fr_m are mainly less than 1, hence the ageostrophic airflow patterns observed in the lowest 3 km are likely induced by blocking from the Sierra. The weaker static stability exhibited during episode 2 produces smaller dry and saturated L_R: ~320 and ~0 km, respectively. While neither of these theoretical estimates matches the location of the southwestern edge of the cross-barrier shear layer, it is notable that both the southwestern edge of the shear layer and L_R are closer to the Sierra crest during episode 2.

The along-barrier RHI at 0655 UTC illustrates the transition from SBJ to AR (Fig. 14). Reflectivity is similar in magnitude to that observed in the cross-barrier RHI, although echo tops are slightly lower (Fig. 14a). A distinct brightband signature is evident, sloping downward to the northwest. At the southeast edge of the cross section near SHS, a thin core of ~20 m s^{-1} U_{340} associated with the SBJ is evident at ~0.5 km MSL (Fig. 14b). About 25 km northwest of SHS the height of maximum U_{340} rises abruptly from ~0.5 to 1.5 km MSL and thickens substantially. Farther northwest, the center height of maximum U_{340} remains approximately constant and its magnitude increases to ~25 m s^{-1}. These structural variations in U_{340} from southeast to northwest correspond well with the U_{340} profiles at SHS (Fig. 14f), LHM (Fig. 14e), and KBBX (Fig. 14d). The profile at CCO (Fig. 14c) is west of the cold front during a large portion of its averaging period, making it inappropriate for comparison to the cross section that is east of the cold front. Although the thin U_{340} maximum at ~0.5 km is not captured by the multiple-Doppler analysis, the thicker maximum at ~1.5 km is clearly seen in Fig. 11i and apparently is associated with the AR. However, this is a

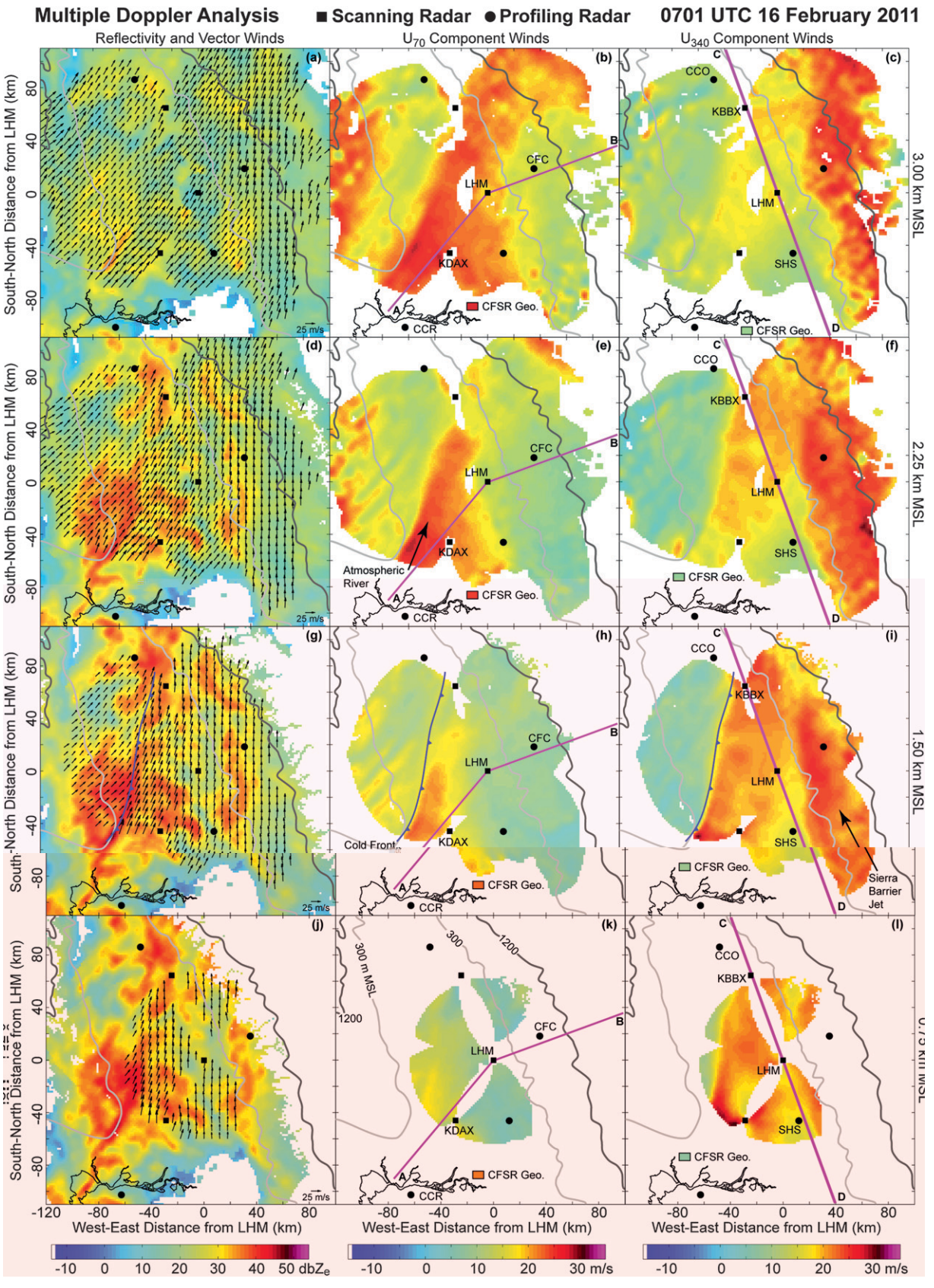
Multiple Doppler Analysis
Scanning Radar
Profiling Radar
0701 UTC 16 February 2011
Reflectivity and Vector Winds
U70 Component Winds
U340 Component Winds
South-North Distance from LHM (km)
West-East Distance from LHM (km)
3.00 km MSL
2.25 km MSL
1.50 km MSL
0.75 km MSL
CCO
KBBX
CFC
LHM
KDAX
SHS
CCR
CFSR Geo.
Atmospheric River
Cold Front
Sierra Barrier Jet
300 m MSL
300
1200
25 m/s
-10 0 10 20 30 40 50 dbZe
-10 0 10 20 30 m/s

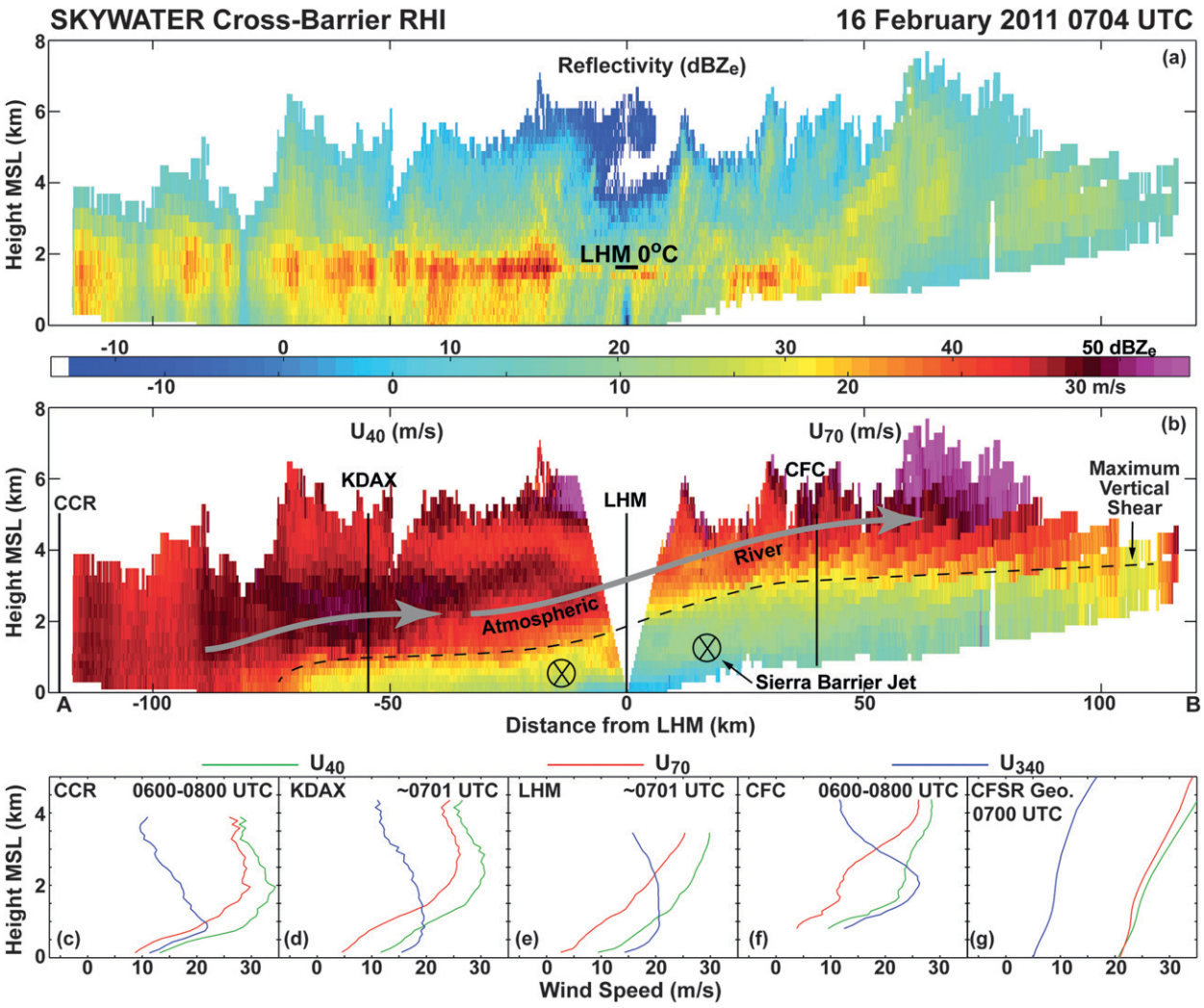

FIG. 12. (a),(b) As in Figs. 7a,b, but at ~0704 UTC 16 Feb. The 0°C level in (a) is derived from an LHM rawinsonde released at 0719 UTC. (c),(f) The CCR and CFC profiles are averaged over the period 0600–0800 UTC. (d),(e) The KDAX and LHM profiles are from ~0701 UTC. (g) CFSR geostrophic profiles are from 0700 UTC.

region where the AR is sloping upward and the SBJ is deepening toward the northeast (Fig. 12b). In this sloping vertical gradient of horizontal airflow, the thick U_{340} maximum at ~1.5 km (Fig. 14b) may be a hybrid of both the AR and SBJ. Indeed, horizontal airflow along this cross section has an ageostrophic component in both the cross- and along-barrier directions, which is apparent examining Figs. 11h,i and by comparing the KDAX and LHM profiles of observed U_{70} and U_{340} with their geostrophic counterparts (Fig. 14g).

5. Summary and conclusions

This study has characterized the kinematic and thermodynamic structures of SBJs, ARs, and their interaction over the period 14–16 February 2011 when a strong winter storm made landfall in northern California. A suite of scanning and profiling Doppler radars, rawinsondes, and GPS receivers was used to document these structures across the Central Valley and up the windward Sierra slope to the crest along an ~200-km segment of

←

FIG. 11. As in Fig. 6, but at ~0701 UTC 16 Feb. The location of the Skywater RHI cross section shown in Fig. 12 is indicated in the center column by magenta line segments A-LHM-B. Likewise, the Skywater RHI cross section shown in Fig. 14 is indicated in the right column by magenta line segments C-LHM-D. The positions of the AR, SBJ, and cold front are indicated.

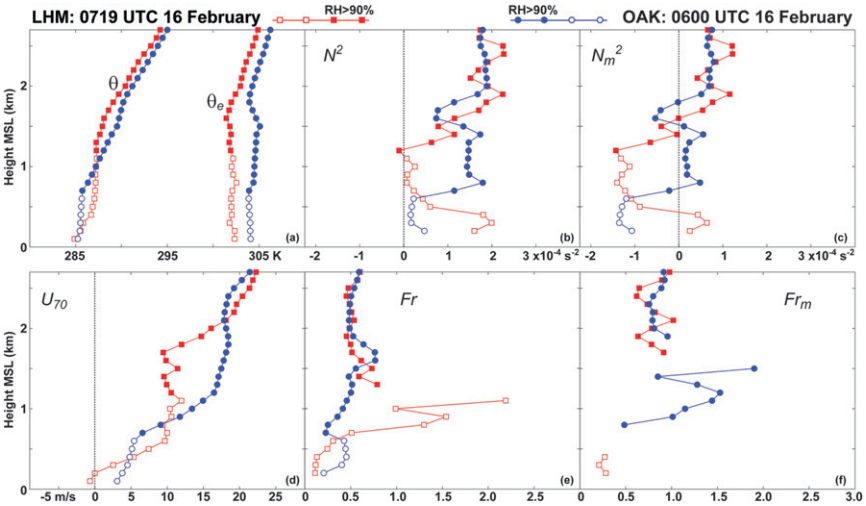

FIG. 13. As in Fig. 8, but for LHM at 0719 UTC 16 Feb and OAK at 0600 UTC 16 Feb.

the Sierra. Three scanning Doppler radars (Skywater, KDAX, and KBBX) were the primary assets as they provided surveillance-scan volumes of reflectivity and radial velocity data over a large portion of northern California, which enabled synthesis of three-dimensional wind fields. In addition, Skywater executed RHI scans oriented both across and along the Sierra, allowing a detailed depiction of SBJ and AR vertical kinematic structure.

The landfalling winter storm investigated in this study was grouped into two episodes. Episode 1 (from 0400 UTC 14 February to 0800 UTC 15 February) was associated with a transient shortwave trough offshore of northern California embedded in a broad cyclonic circulation at 500 hPa centered over the Gulf of Alaska. It was accompanied by a long, narrow filament of enhanced vertically integrated water vapor flux indicative of an AR. Episode 2 (from 1400 UTC 15 February to 1800 UTC 16 February) was associated with a second AR making landfall in northern California during the eastward progression of the parent Gulf of Alaska cyclone. The dynamics with episode 2 were stronger and accompanied by a cold front. In addition, the cross-barrier bulk IWV flux was larger during episode 2, which likely contributed to the deeper, more widespread, and higher-valued radar reflectivity and larger surface rainfall rates and accumulations observed during this period compared to episode 1.

A schematic that summarizes the kinematic characteristics of SBJs and ARs during both episodes is presented in Fig. 15. The SBJ was defined by low-level south-southeasterly winds of 20–30 m s^{-1}. These winds were stronger and had a larger easterly component during episode 1 compared to episode 2. The altitude of maximum U_{340} was as low as ~0.2 km MSL over the Central Valley and as high as ~1.5 km MSL (episode 1) and ~2.5 km MSL (episode 2) over the western Sierra slope. In addition, the height and layer thickness of maximum U_{340} increased from southeast to northwest. Southwesterly winds of ~20–30 m s^{-1} associated with the AR extended over the SBJ along an interface that sloped upward from southwest to northeast, ~1%–2% during episode 1 and ~2%–4% during episode 2. The southwestern extent of this sloping interface was at the western edge of the Central Valley during episode 1, but only to the western half of the Central Valley during episode 2.

Airflow associated with the SBJ was ageostrophic in the lowest 3 km, indicative of a cross-barrier airstream blocked by the Sierra and deflected leftward in an along-barrier direction. The SBJ air mass was stably stratified during both episodes, but more strongly during episode 1. In addition, Fr and Fr_m were both mainly less than 1, with smaller values observed during episode 1. These factors suggest that blocking is a likely explanation for the observed ageostrophic airflow patterns observed in the lowest 3 km.

This study has extended previous SBJ research results by providing unique insights into SBJ structure west of the Sierra across the Central Valley and along a significant portion of the northern Sierra. In particular, the results show that the SBJ acts as a virtual barrier, providing a means to lift moisture-laden air parcels along sloping isentropic surfaces in the AR well upstream of the Sierra. This has the potential to initiate or enhance precipitation over the Central Valley and western Sierra. Although Marwitz (1983, 1987) inferred this type of structure from their relatively limited observations,

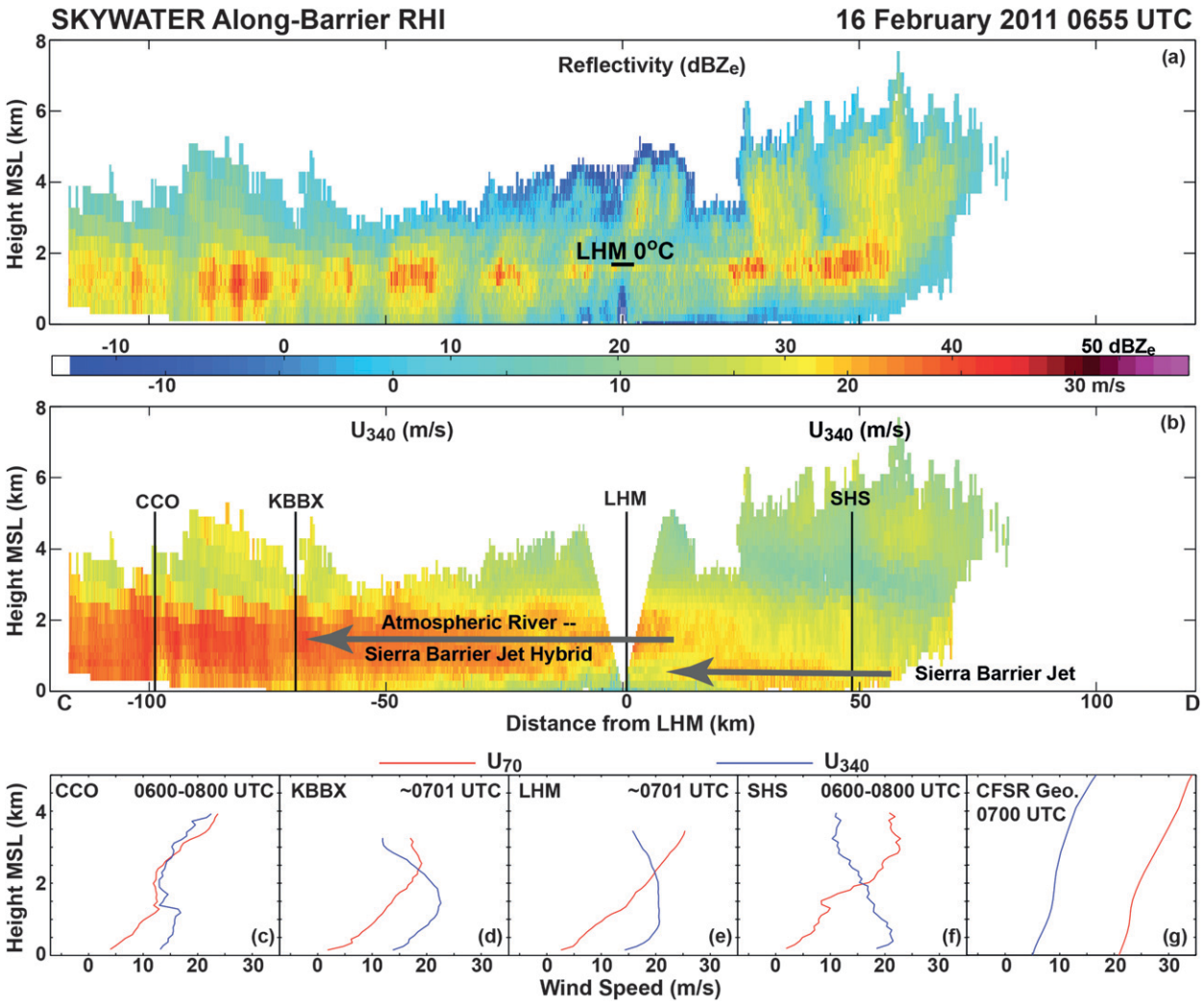

FIG. 14. (a),(b) As in Figs. 9a,b, but at ~0655 UTC 16 Feb. The 0°C level in (a) is derived from an LHM rawinsonde released at 0719 UTC. (c),(f) The CCO and SHS profiles are averaged over the period 0600–0800 UTC. (d),(e)The KBBX and LHM profiles are from ~0701 UTC. (g) CFSR geostrophic profiles are from 0700 UTC.

the present study has unambiguously documented a virtual barrier from a kinematic standpoint along the western Central Valley to the western Sierra slopes. Similar structures have been comparably documented in association with the Alps (Bousquet and Smull 2003; Medina et al. 2005), the Wasatch (Cox et al. 2005), and the Cascades (Medina et al. 2005; Garvert et al. 2007).

However, several questions remain. One of these relates to the western extent of the SBJ and factors that modulate its location. In both episodes of this study, the SBJ extended no further than the western edge of the Central Valley. However, this was only near the coastal-mountain gap; SBJ western extent to the north and south may be different. Theoretical estimates using dry L_R derived from rawinsondes launched at LHM indicate that blocking effects from the Sierra should extend out to the Pacific Ocean. Saturated L_R from these soundings matches well with western SBJ extent for episode 1, but suggests no blocking should occur for episode 2. Obviously, L_R calculated from a single rawinsonde location is not adequate for explaining SBJ western extent. A more comprehensive mapping of thermodynamic characteristics across the Central Valley and westward to the coast is likely needed to advance understanding of this issue. Another question deals with influences that control SBJ depth and thickness across and along the Sierra. As earlier hypothesized, spatial variations in diabatic cooling could be a factor. Testing this hypothesis also requires better mapping of thermodynamics. Additionally, terrain characteristics in the area could be a factor. Specifically, how do the coastal mountains, the coastal-mountain gap and concave and convex segments of the

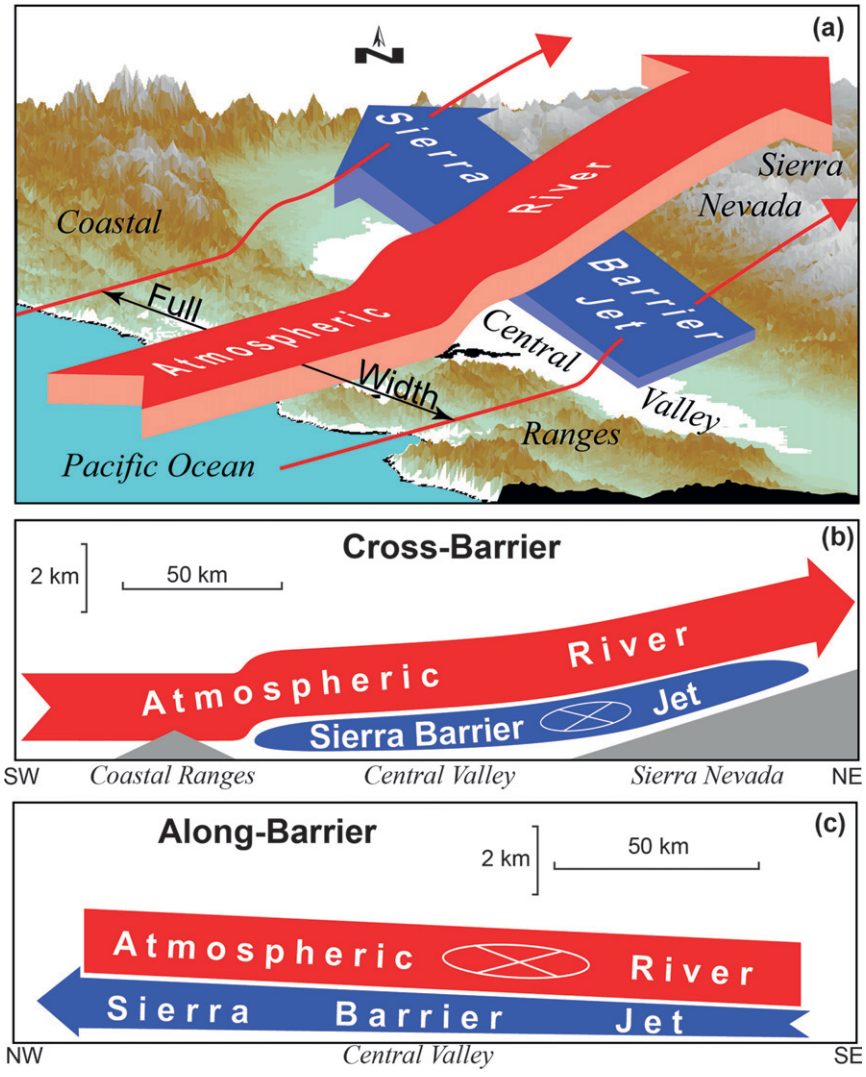

FIG. 15. Schematic illustrations from (a) three-dimensional, (b) cross-barrier two-dimensional, and (c) along-barrier two-dimensional perspectives that depict the kinematic structures of SBJs and ARs observed during this study.

Sierra influence SBJ depth and thickness? Future studies by the authors will explore these and other unresolved questions about the SBJ.

Acknowledgments. The authors thank the NOAA/ESRL observing systems team for deploying and operating the instrumentation whose data were employed in this study. We also acknowledge NOAA/NWS for providing supplemental soundings from Oakland and granting our request to operate the KDAX and KBBX WSR-88D radars in VCP-12. Jim Means of Scripps provided spatial analyses of GPS-derived integrated water vapor that provided important context for this study. Gary Wick of ESRL generated the serial rawinsonde analyses that were used to create Fig. 4. Figures 5 and 10 were skillfully drafted by Jim Adams. We appreciate the comments and suggestions of Ellen Sukovich and Ola Persson of ESRL and two anonymous reviewers on earlier versions of this manuscript. This research and the associated data collection were supported jointly by NOAA and the California Energy Commission.

REFERENCES

Bousquet, O., and B. F. Smull, 2003: Observations and impacts of upstream blocking during a widespread orographic precipitation event. *Quart. J. Roy. Meteor. Soc.,* **129,** 391–409.

Braun, S. A., R. A. Houze Jr., and B. F. Smull, 1997: Airborne dual-Doppler observations of an intense frontal system

approaching the Pacific Northwest coast. *Mon. Wea. Rev.,* **125,** 3131–3156.

Brown, R. A., R. M. Steadham, B. A. Flickinger, R. R. Lee, D. Sirmans, and V. T. Wood, 2005: New WSR-88D volume coverage pattern 12: Results of field tests. *Wea. Forecasting,* **20,** 385–393.

Browning, K. A., 1990: Organization of clouds and precipitation in extratropical cyclones. *Extratropical Cyclones: The Erik H. Palmén Memorial Volume,* C. Newton and E. Holopainen, Eds., Amer. Meteor. Soc., 129–153.

——, and R. Wexler, 1968: The determination of kinematic properties of a wind field using Doppler radar. *J. Appl. Meteor.,* **7,** 105–113.

Carbone, R. E., M. J. Carpenter, and C. D. Burghart, 1985: Doppler radar sampling limitations in convective storms. *J. Atmos. Oceanic Technol.,* **2,** 357–361.

Carlson, T. N., 1998: *Mid-Latitude Weather Systems.* Amer. Meteor. Soc., 507 pp.

Carter, D. A., K. S. Gage, W. L. Ecklund, W. M. Angevine, P. E. Johnston, A. C. Riddle, J. S. Wilson, and C. R. Williams, 1995: Developments in UHF lower-tropospheric wind profiling at NOAA's Aeronomy Laboratory. *Radio Sci.,* **30,** 997–1001.

Cox, J. A. W., W. J. Steenburgh, D. E. Kingsmill, J. C. Shafer, B. A. Colle, O. Bousquet, B. F. Smull, and H. Cai, 2005: The kinematic structure of a Wasatch Mountain winter storm during IPEX IOP3. *Mon. Wea. Rev.,* **133,** 521–542.

Crum, T. D., R. L. Alberty, and D. W. Burgess, 1993: Recording, archiving, and using WSR-88D data. *Bull. Amer. Meteor. Soc.,* **74,** 645–653.

Doyle, J. D., 1997: The influence of mesoscale orography on a coastal jet and rainband. *Mon. Wea. Rev.,* **125,** 1465–1488.

Duan, J., and Coauthors, 1996: GPS meteorology: Direct estimation of the absolute value of precipitable water vapor. *J. Appl. Meteor.,* **35,** 830–838.

Durran, D. R., and J. B. Klemp, 1982: On the effects of moisture on the Brunt–Väisälä frequency. *J. Atmos. Sci.,* **39,** 2152–2158.

Friedrich, K., D. E. Kingsmill, C. Flamant, H. V. Murphey, and R. M. Wakimoto, 2008: Kinematic and moisture characteristics of a nonprecipitating cold front observed during IHOP. Part II: Along front structures. *Mon. Wea. Rev.,* **136,** 3796–3821.

Galewsky, J., and A. Sobel, 2005: Moist dynamics and orographic precipitation in northern and central California during the New Year's Flood of 1997. *Mon. Wea. Rev.,* **133,** 1594–1612.

Garvert, M. F., B. Smull, and C. Mass, 2007: Multiscale mountain waves influencing a major orographic precipitation event. *J. Atmos. Sci.,* **64,** 711–737.

Houser, J. L., and H. B. Bluestein, 2011: Polarimetric Doppler radar observations of Kelvin–Helmholtz waves in a winter storm. *J. Atmos. Sci.,* **68,** 1676–1702.

Kessinger, C. J., P. S. Ray, and C. E. Hane, 1987: The 19 May 1977 Oklahoma squall line. Part I: A multiple-Doppler analysis of convective and stratiform structure. *J. Atmos. Sci.,* **44,** 2840–2864.

Leise, J. A., 1982: A multidimensional scale-telescoped filter and data extension package. NOAA Tech. Memo. ERL WPL-82, 19 pp. [Available from NOAA/ESRL, 325 Broadway, Boulder, CO 80305.]

Loescher, K. A., G. S. Young, B. A. Colle, and N. S. Winstead, 2006: Climatology of barrier jets along the Alaskan coast. Part I: Spatial and temporal distributions. *Mon. Wea. Rev.,* **134,** 437–453.

Lundquist, J. D., J. R. Minder, P. J. Neiman, and E. Sukovich, 2010: Relationships between barrier jet heights, orographic precipitation gradients, and streamflow in the northern Sierra Nevada. *J. Hydrometeor.,* **11,** 1141–1156.

Marwitz, J., 1983: The kinematics of orographic airflow during Sierra storms. *J. Atmos. Sci.,* **40,** 1218–1227.

——, 1987: Deep orographic storms over the Sierra Nevada. Part I: Thermodynamic and kinematic structure. *J. Atmos. Sci.,* **44,** 159–173.

Medina, S., B. F. Smull, R. A. Houze Jr., and M. Steiner, 2005: Cross-barrier flow during orographic precipitation events: Results from MAP and IMPROVE. *J. Atmos. Sci.,* **62,** 3580–3598.

Minder, J. R., and D. E. Kingsmill, 2013: Mesoscale variations of the atmospheric snow line over the northern Sierra Nevada: Multiyear statistics, case study, and mechanisms. *J. Atmos. Sci.,* **70,** 916–938.

——, D. R. Durran, and G. H. Roe, 2011: Mesoscale controls on the mountainside snow line. *J. Atmos. Sci.,* **68,** 2107–2127.

Neiman, P. J., F. M. Ralph, A. B. White, D. E. Kingsmill, and P. O. G. Persson, 2002: The statistical relationship between upslope flow and rainfall in California's coastal mountains: Observations during CALJET. *Mon. Wea. Rev.,* **130,** 1468–1492.

——, P. O. G. Persson, F. M. Ralph, D. P. Jorgensen, A. B. White, and D. E. Kingsmill, 2004: Modification of fronts and precipitation by coastal blocking during an intense landfalling winter storm in Southern California: Observations during CALJET. *Mon. Wea. Rev.,* **132,** 242–273.

——, F. M. Ralph, A. B. White, D. D. Parrish, J. S. Holloway, and D. L. Bartels, 2006: A multiwinter analysis of channeled flow through a prominent gap along the northern California coast during CALJET and PACJET. *Mon. Wea. Rev.,* **134,** 1815–1841.

——, ——, G. A. Wick, J. Lundquist, and M. D. Dettinger, 2008: Meteorological characteristics and overland precipitation impacts of atmospheric rivers affecting the west coast of North America based on eight years of SSM/I satellite observations. *J. Hydrometeor.,* **9,** 22–47.

——, A. B. White, F. M. Ralph, D. J. Gottas, and S. I. Gutman, 2009: A water vapor flux tool for precipitation forecasting. *Proc. Inst. Civil Eng. (Water Manage.),* **162,** 83–94.

——, E. M. Sukovich, F. M. Ralph, and M. Hughes, 2010: A seven-year wind profiler–based climatology of the windward barrier jet along California's northern Sierra Nevada. *Mon. Wea. Rev.,* **138,** 1206–1233.

Olson, J. B., and B. A. Colle, 2009: Three-dimensional idealized simulations of barrier jets along the southeast coast of Alaska. *Mon. Wea. Rev.,* **137,** 391–413.

——, ——, N. A. Bond, and N. Winstead, 2007: A comparison of two coastal barrier jet events along the southeast Alaskan Coast during the SARJET field experiment. *Mon. Wea. Rev.,* **135,** 3642–3663.

Overland, J. E., and N. A. Bond, 1995: Observations and scale analysis of coastal wind jets. *Mon. Wea. Rev.,* **123,** 2934–2941.

Parish, T. R., 1982: Barrier winds along the Sierra Nevada Mountains. *J. Appl. Meteor.,* **21,** 925–930.

Pierrehumbert, R. T., and B. Wyman, 1985: Upstream effects of mesoscale mountains. *J. Atmos. Sci.,* **42,** 977–1003.

Ralph, F. M., P. J. Neiman, and G. A. Wick, 2004: Satellite and CALJET aircraft observations of atmospheric rivers over the eastern North Pacific Ocean during the winter of 1997/98. *Mon. Wea. Rev.,* **132,** 1721–1745.

——, ——, and R. Rotunno, 2005a: Dropsonde observations in low-level jets over the northeastern Pacific Ocean from CALJET-1998 and PACJET-2001: Mean vertical-profile

and atmospheric-river characteristics. *Mon. Wea. Rev.,* **133,** 889–910.

——, and Coauthors, 2005b: Improving short term (0–48 h) cool season quantitative precipitation forecasting: Recommendations from a USWRP workshop. *Bull. Amer. Meteor. Soc.,* **86,** 1619–1632.

Reeves, H. D., Y.-L. Lin, and R. Rotunno, 2008: Dynamic forcing and mesoscale variability of heavy precipitation events over the Sierra Nevada Mountains. *Mon. Wea. Rev.,* **136,** 62–77.

Reynolds, D. W., and A. S. Dennis, 1986: A review of the Sierra Cooperative Pilot Project. *Bull. Amer. Meteor. Soc.,* **67,** 513–523.

Saha, S., and Coauthors, 2010: The NCEP Climate Forecast System Reanalysis. *Bull. Amer. Meteor. Soc.,* **91,** 1015–1057.

Smith, B. L., S. E. Yuter, P. J. Neiman, and D. E. Kingsmill, 2010: Water vapor fluxes and orographic precipitation over northern California associated with a landfalling atmospheric river. *Mon. Wea. Rev.,* **138,** 74–100.

Smolarkiewicz, P. K., and R. Rotunno, 1990: Low Froude number flow past three-dimensional obstacles. Part II: Upwind flow reversal zone. *J. Atmos. Sci.,* **47,** 1498–1511.

Smutz, S. W., 1986: A climatology of the Sierra Nevada barrier jet. M.S. thesis, Paper AS-153, Dept. of Atmospheric Science, University of Wyoming, Laramie, WY, 108 pp.

Steiner, M., O. Bousquet, R. A. Houze Jr., B. F. Smull, and M. Mancini, 2003: Airflow within major Alpine river valleys under heavy rainfall. *Quart. J. Roy. Meteor. Soc.,* **129,** 411–431.

Weber, B. L., D. B. Wuertz, D. C. Welsh, and R. McPeek, 1993: Quality controls for profiler measurements of winds and RASS temperatures. *J. Atmos. Oceanic Technol.,* **10,** 452–464.

Wentz, F. J., 1995: The intercomparison of 53 SSM/I water vapor algorithms. Remote Sensing Systems Tech. Rep. on WetNet Water Vapor Intercomparison Project (VIP), Santa Rosa, CA, 19 pp.

Wolfe, D. E., and S. I. Gutman, 2000: Developing an operational, surface-based, GPS, water vapor observing system for NOAA: Network design and results. *J. Atmos. Oceanic Technol.,* **17,** 426–440.

Yu, C.-K., and N. A. Bond, 2002: Airborne Doppler observations of a cold front in the vicinity of Vancouver Island. *Mon. Wea. Rev.,* **130,** 2692–2708.

——, and B. F. Smull, 2000: Airborne Doppler observations of a landfalling cold front upstream of steep coastal orography. *Mon. Wea. Rev.,* **128,** 1577–1603.

Zhu, Y., and R. E. Newell, 1998: A proposed algorithm for moisture fluxes from atmospheric rivers. *Mon. Wea. Rev.,* **126,** 725–735.